FOREWORD

This report was prepared by The University of Michigan under USAF Contract No. AF33(657)-7531 and describes research accomplished during the period from 1 January 1962 to 28 February 1964. The contract was initiated under Project No. 7353, "Characterization of Solid Phase and Interphase Phenomena in Crystalline Substances," Task No. 735301, "Mechanical Metallurgy."

The work was under the direction of the Directorate of Materials and Processes, Deputy Commander/Technology, Aeronautical Systems Division, with Dr. J. A. Herzog acting as project engineer.

ABSTRACT

Experimental initial yield, strain hardening, and fracture data for arc-cast unalloyed molybdenum tubular specimens are compared with simple theoretical models. The tubular specimens were subjected to various combinations of axial force and internal pressure at testing temperatures of 75°F and 212°F. Initial yield data are in fairly good agreement with a maximum reduced stress yield criterion which accounts for axially symmetric anisotropy. The theory of kinematic hardening gave good predictions of subsequent yield values during strain hardening for the 75°F data. For tests at 212°F, markedly poorer predictions of subsequent yield were given. A maximum normal stress theory of fracture was in fair agreement with experimental data.

Data are also presented on the behavior of cantilever beams made of Zamak-3 zinc alloy. Strain hardening in Zamak-3 had been investigated previously. These results are in reasonably good agreement with a theoretical load-tip deflection relationship based on an elastic-linear strain hardening model.

This technical documentary report has been reviewed and is approved.

W. G. RAMKE, ACTING CHIEF
ADVANCED METALLURGICAL STUDIES BRANCH
METALS AND CERAMICS DIVISION
AF MATERIALS LABORATORY

TABLE OF CONTENTS

LIST OF FIGURES

LIST OF FIGURES (Concluded)

INTRODUCTION

The present report is divided into two parts because of the distinctly different purposes of the two phases of the research.

In Part I, the behavior of unalloyed, arc-cast molybdenum in the plastic range is investigated from an experimental viewpoint. The test results are used to determine whether a simple theoretical model of material behavior is valid.

Part II, on the other hand, contains the application of linear strain hardening theory to a one-dimensional structure. This theoretical development is compared to experiments made on members of Zamak-3, zinc alloy whose properties for the plastic range have been reported previously.

Manuscript released by authors March 31, 1964 for publication as an ASD Technical Documentary Report.

PART I

PLASTIC BEHAVIOR OF ARC-CAST MOLYBDENUM

This part of the report describes an experimental investigation of initial yielding, strain hardening, and fracture in arc-cast molybdenum, tubular specimens at two testing temperatures.

The experimental data are compared with the predictions of a simple kinematic theory of strain hardening in which an anisotropic initial yield condition is employed. This approach had given relatively good results for an isotropic material, Zamak-3 zinc alloy in previous work (see WADD-TR-60-869, Part II).[1] Further, kinematic hardening theory is attractive since it is simple enough to use in the solution of boundary value problems, and thus a means is available to extend the results to more general applications. For fracture, data are compared with the criterion of Griffith (see WADD-TR-60-869, Part II).[1] This latter is, in effect, a maximum normal stress theory for the range of states of stress covered.

The test material is an unalloyed, arc-cast molybdenum which is available under the trade name Climelt (R). Its composition is:

Element	Percent
M_o	> 99.9
C	0.022
O^2	< 0.0002
H^2	< 0.0001
N^2	0.0001
Fe	< 0.001
Ni	< 0.001
Si	< 0.003

Specimens were cut from 1-1/8-inch diameter, wrought bar stock which was furnished in the stress-relieved (heated 1-1/4-hour at 1750°F) condition.

There is evidence of plastic working of the material, probably during forming of the bar stock, as shown in the photomicrographs, Figure 1. These photomicrographs represent longitudinal sections through the tube wall and do indicate elongation of grains in the direction of the tube axis which is also the bar axis. Data which are presented later indicate that the material is anisotropic with regard to behavior in the plastic range. It is supposed that the observed anisotropy is related to the elongated grain structure.

Specimens used in obtaining the data reported here were of the type shown

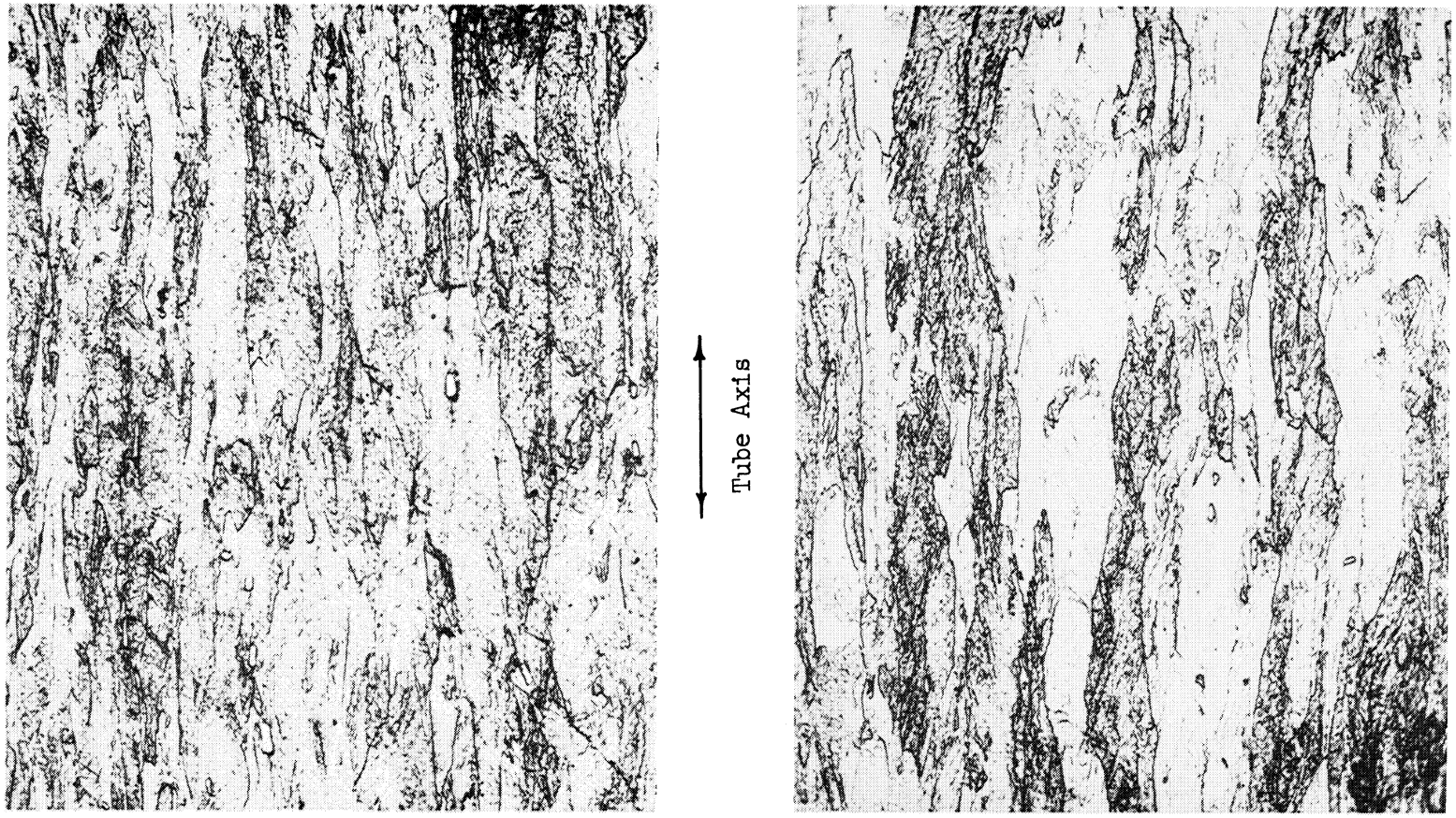

Figure 1. Grain structure of molybdenum on a longitudinal section through tube wall.

in Figure 2. These tubular specimens were subjected to combinations of axial force and internal pressure and the stresses in the thin-walled tube are statically determinate for these loads. The stresses are:

$$\sigma_z = \frac{P}{2\pi rt} + \frac{pr}{2t}$$

$$\sigma_\theta = \frac{pr}{t} \qquad (1.1)$$

$$\sigma_r = \tau_{r\theta} = \tau_{\theta z} = \tau_{rz} = 0$$

where

r = mean radius of tube
t = wall thickness
P = axial force
p = internal pressure
σ_z = axial stress
σ_θ = circumferential stress.

Note that all normal stresses are principal stresses and that the radial stress, σ_r, is assumed zero. The principal directions of stress remain fixed in an element of the material for all load combinations.

All tests were conducted in the combined load testing machine which is described completely in WADD-TR-60-234.[2] Although the machine has been modified somewhat the general features are the same as originally reported. The principal refinement in the load application system is that the axial loading system and the internal pressure system have been uncoupled. Thus it is possible to follow nonproportional loading and unloading paths. Further an arbitrary change in the loading path during a test run is permitted. Another refinement in the axial loading system is the addition of universal joints at points immediately above and below the specimen to assure axiality of load application. In addition to the above, a 10:1 pressure intensifier has been installed in the internal pressure system so that controlled internal pressures up to 15,000 psi can be obtained.

Finally, tests at 212°F were carried out by immersing the specimen in a tank containing oil heated by conventional immersion heaters. The tank itself is not a new item of equipment since it was used for some of the Zamak-3 tests. It encloses the specimen and universal joints and is attached to the lower specimen grip.

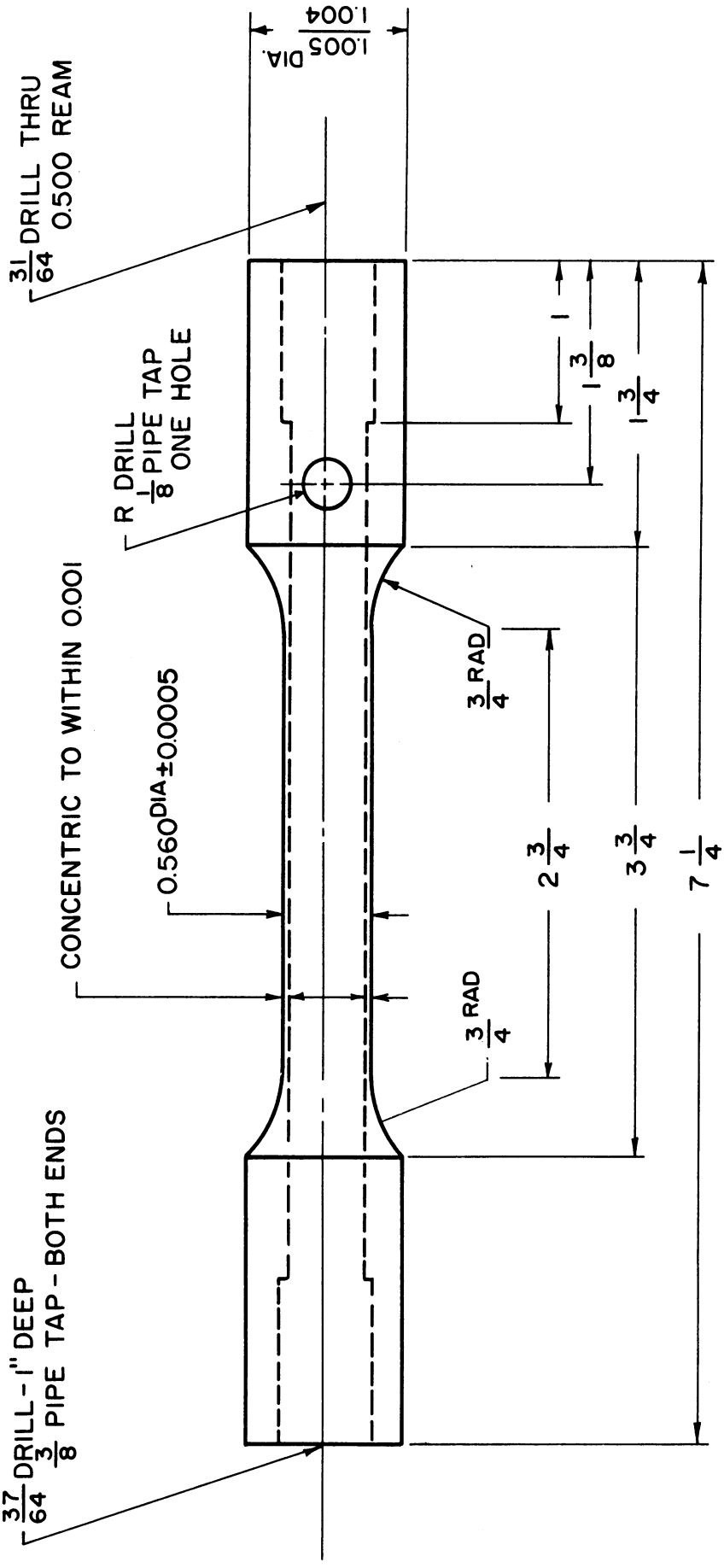

Figure 2. Sketch of Tubular Specimen

A. INITIAL YIELDING

For the experimental conditions considered in this research program, arc-cast molybdenum is typified by a stress-strain curve with a continuously turning tangent. Representative stress-strain curves are shown in Figure 3 for 75°F and in Figure 4 for 212°F. Both of these sets of data were obtained by subjecting tubular specimens to tensile axial loads. Rates of loading were quite slow. For example, the time to reach a stress of 70,000 psi was 30 minutes or longer. It should be pointed out that some data have been reported which suggest a drop in stress after yielding. However, such data were obtained at much higher rates of loading.

In this investigation, the yield stress or state of stress at yielding was defined as the proportional limit state of stress, that is the state of stress at which a plot of representative stress versus representative strain deviates from linearity. The correctness of the proportional limit stress as an indicator of the onset of plastic deformation is demonstrated in Figures 5 and 6. Data for Figure 5 were obtained by loading in tension to a point beyond the proportional limit and then unloading to check for permanent strain. The procedure was then repeated. It can be observed that loading to a stress beyond the proportional limit stress for each cycle does induce plastic deformation. Unloading is linearly elastic as expected. The results presented in Figure 6 show that for internal pressure only essentially the same results are obtained.

At temperature of 75° and 212°F, arc-cast molybdenum would not be expected to show creep or other time-dependent behavior. This point was checked in several instances of combined loading and no evidence of creep was observed when the loading was held fixed for periods of 4 to 5 minutes.

Initial yield in molybdenum tubes appears to be anisotropic. This is indicated in data for 75°F which are shown in Figure 7, a plot of the octahedral plane of principal stress space. The x-y coordinates in the octahedral plane are related to the stresses σ_z and σ_θ ($\sigma_r = 0$) by

$$x = \frac{1}{\sqrt{2}} (-\sigma_z + \sigma_\theta)$$

$$y = -\frac{1}{\sqrt{6}} (\sigma_z + \sigma_\theta)$$

It is also clear from Figure 7 that there is considerable scatter in data from specimen to specimen. Values of stress at yield on the σ_z-axis (pure tension) range from σ_z = 35,300 psi to 43,100 psi with σ_θ equal to zero in all cases. Values of stress at yield along the radial line $\sigma_\theta = 2\sigma_z$ (pure internal pressure) range from σ_θ = 46,600 psi, σ_z = 23,300 psi to σ_θ = 61,900 psi, σ_z

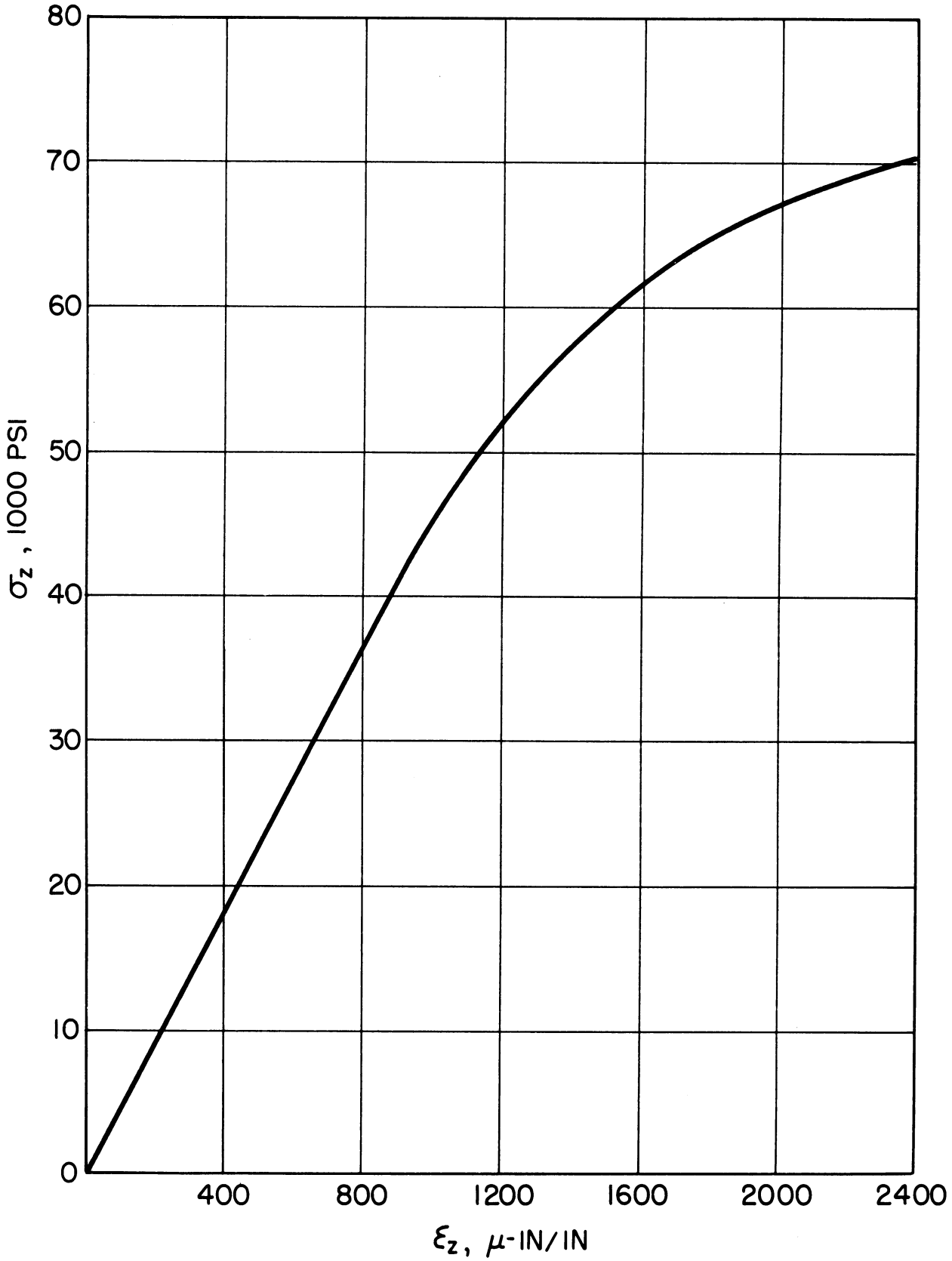

Figure 3. Tension Stress-Strain Curve. 75°F Test MPP-9, L-3

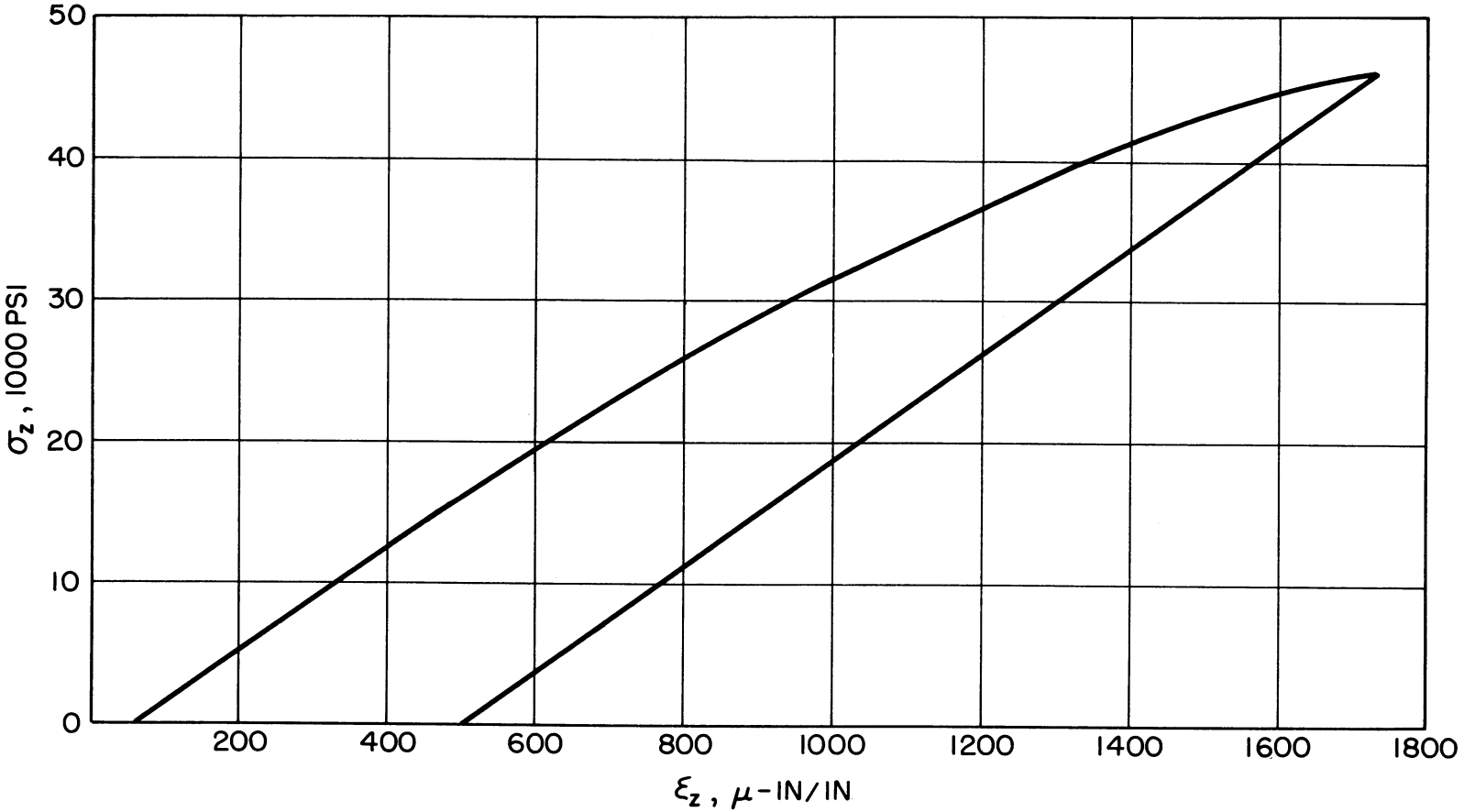

Figure 4. Tension Stress-Strain Curve. 212°F Test MPP-16, L-1

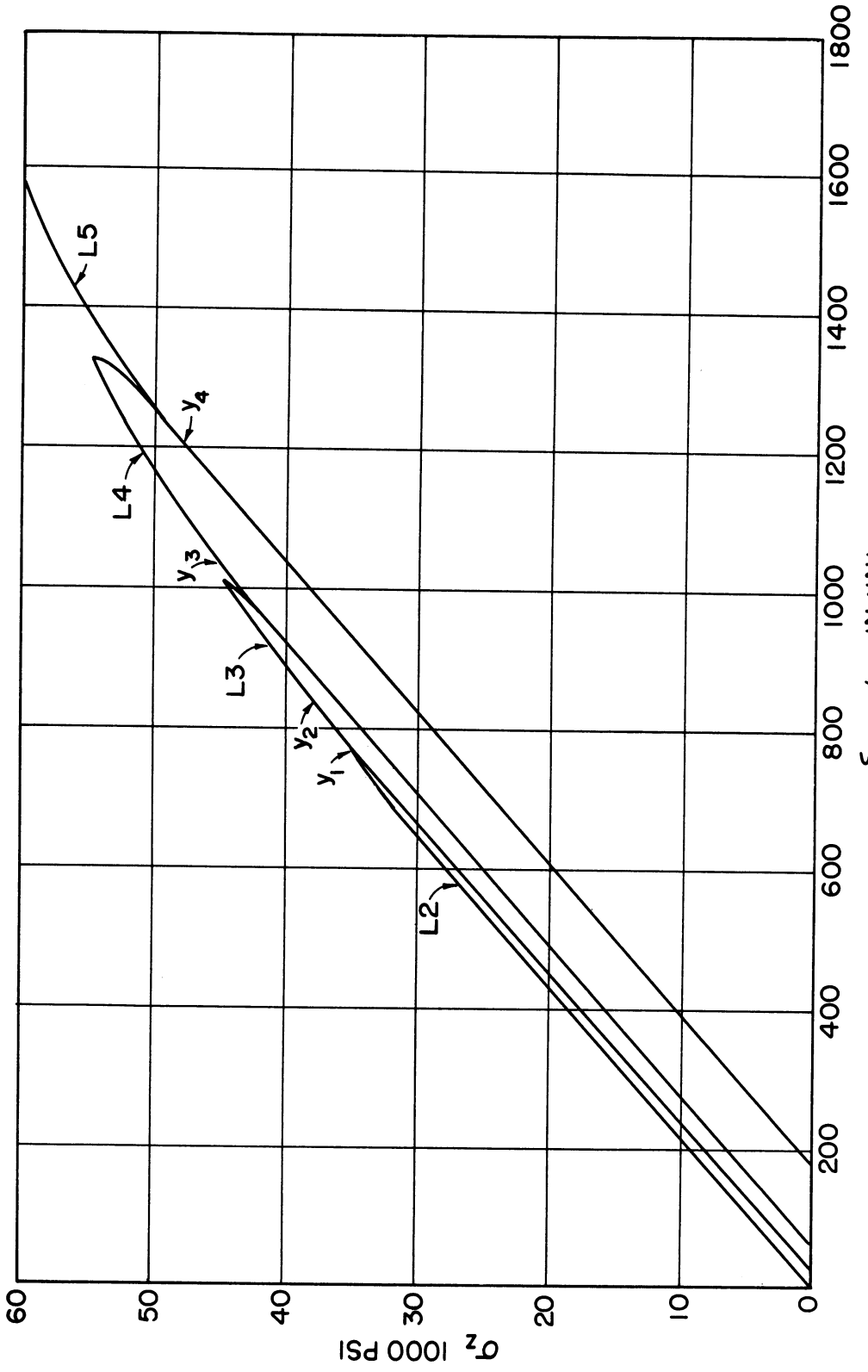

Figure 5. Load-Unload Tension Test. MPO-3

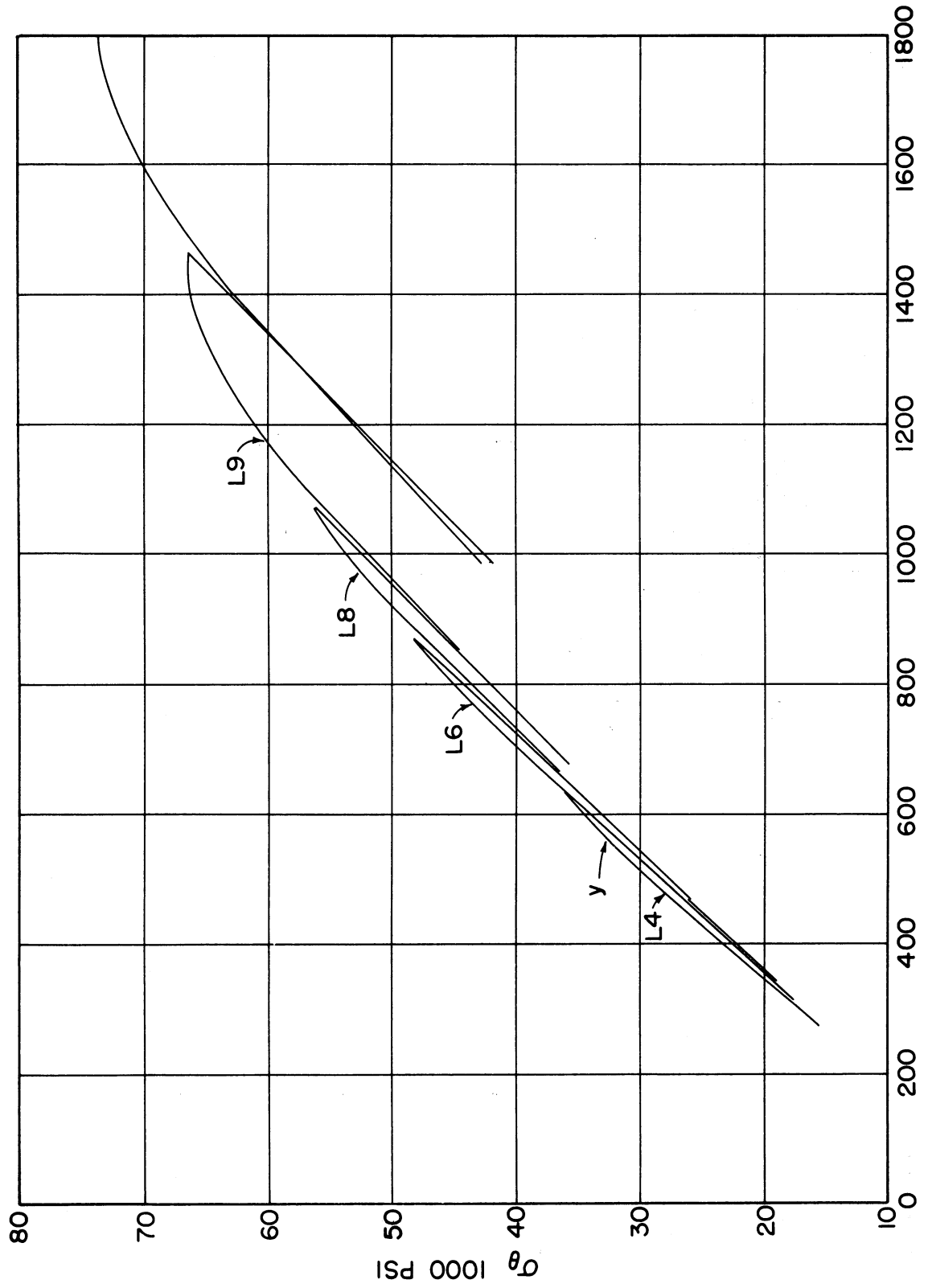

Figure 6. Load-Unload Internal Pressure Test. MPO-2

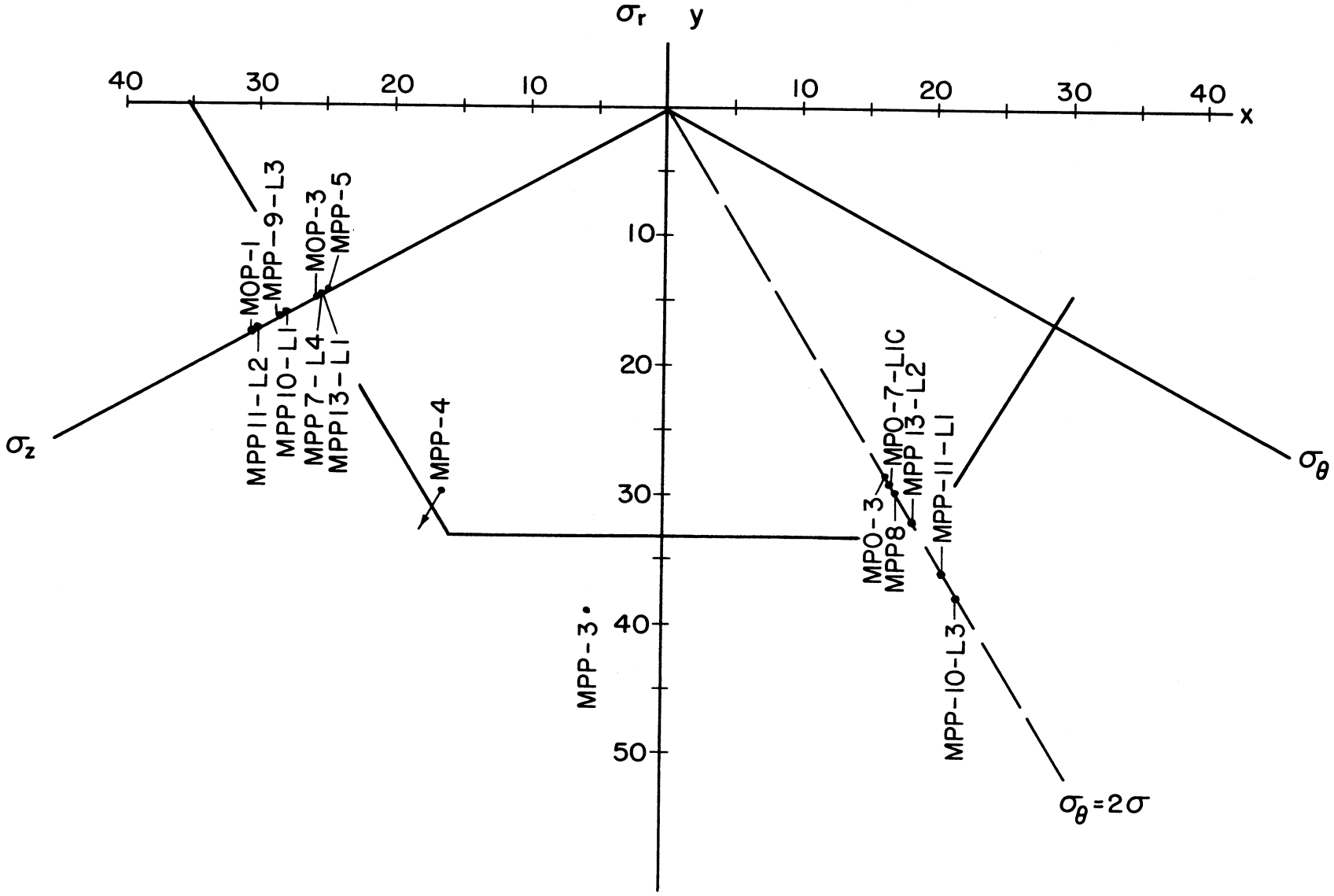

Figure 7. Initial Yield Data at 75°F

= 30,500 psi. It is noted that similar values were obtained at 212°F.

Now let us return to the apparent anisotropy. The degree of anisotropy depends on the specific yield criterion which is used. However, the Tresca, the von Mises, and the maximum reduced stress yield criteria all indicate some anisotropy. In this analysis, assume that all three criteria are forced to agree for pure tension and that the yield stress is 39,000 psi. Then for points on $\sigma_\theta = 2\sigma_z$: the isotropic Tresca criterion gives σ_θ = 39,000 psi, σ_z = 19,500 psi; the isotropic von Mises criterion gives σ_θ = 45,000 psi, σ_z = 22,500 psi; and the isotropic maximum reduced stress criterion gives σ_θ = 52,000, σ_z = 26,000 psi. The isotropic forms of these yield criteria are:

Tresca

$$\max \left\{ |\sigma_z - \sigma_r|, |\sigma_\theta - \sigma_z|, |\sigma_\theta - \sigma_r| \right\} = \sigma_o \qquad (1.2a)$$

von Mises

$$(\sigma_z - \sigma_r)^2 + (\sigma_\theta - \sigma_z)^2 + (\sigma_\theta - \sigma_r)^2 = 2\sigma_o^2 \qquad (1.2b)$$

and maximum reduced stress[3]

$$\max \left\{ |\sigma_z - \sigma|, |\sigma_r - \sigma|, |\sigma_\theta - \sigma| \right\} = \frac{2}{3}\sigma_o \qquad (1.2c)$$

where σ_o is the yield stress and σ is the average normal stress. It can be seen from the above computed values that isotropic yield criteria would all predict values for yielding on $\sigma_\theta = 2\sigma_z$ which are smaller than the observed values. Thus anisotropic forms of the yield criteria are required in order to account for a yield stress in the circumferential direction of a tube that is larger than the yield stress in the axial direction of a tube.

In what follows it is assumed that the principal axes of anisotropy are the r-, θ-, z- directions of the tube and that anisotropy is axially symmetric. The latter implies that σ_θ^*, the yield stress in the circumferential direction, is equal to σ_r^*, the yield stress in the radial direction. The three yield criteria used above can be adapted to this type of anisotropy. The Tresca criterion is

$$
\begin{aligned}
|\sigma_z - \sigma_r| &= \sigma_z^* \\
|\sigma_z - \sigma_\theta| &= \sigma_z^* \\
|\sigma_\theta - \sigma_r| &= \sigma_\theta^*
\end{aligned}
\tag{1.3}
$$

where σ_z^* is the yield stress in the axial direction. For von Mises we have

$$
A(\sigma_z - \sigma_r)^2 + A(\sigma_\theta - \sigma_z)^2 + B(\sigma_\theta - \sigma_r)^2 = 1 \tag{1.4}
$$

where

$$
\frac{1}{(\sigma_z^*)^2} = 2A; \quad \frac{1}{(\sigma_\theta^*)^2} = A + B; \quad \frac{1}{(\sigma_r^*)^2} = A + B \quad .
$$

Finally the maximum reduced stress criterion becomes

$$
\begin{aligned}
|\sigma_z - \sigma| &= \frac{2}{3}\sigma_z^* \\
|\sigma_r - \sigma| &= \frac{2}{3}\sigma_r^* \\
|\sigma_\theta - \sigma| &= \frac{2}{3}\sigma_\theta^* \quad .
\end{aligned}
\tag{1.5}
$$

In Equations (1.3), yielding is said to occur as soon as one of the equations is satisfied. The same is true of Equations (1.5).

In regard to the assumption of axially symmetric anisotropy, a partial justification is possible. This is based on data obtained from tubes loaded in pure tension. Plastic axial and circumferential strains observed in this way can give evidence of anisotropy in conjunction with the anisotropic von Mises yield criterion, Equation (1.4). Applying the flow rule,

$$
d\epsilon_{ij}^P = x \frac{\partial F(\sigma_{ij})}{\partial \sigma_{ij}} \tag{1.6}
$$

in which $F(\sigma_{ij})$ is the yield function, to Equation (1.4) we find that

$$
\frac{d\epsilon_\theta{}^P}{d\epsilon_z{}^P} = -\frac{1}{2} \tag{1.7}
$$

when all stresses except for σ_z are equal to zero. This is supported reasonably well by test results since in MPP5-L1 the above ratio is -0.4647 and in MPP2-L1 the ratio is -0.4158. If σ_θ^* were not equal to σ_r^*, instead of Equation (1.7), we would obtain

$$\frac{d\epsilon_\theta^P}{d\epsilon_z^P} = -1 + \frac{1}{2}\left(\frac{\sigma_\theta^*}{\sigma_r^*}\right)^2 . \qquad (1.8)$$

The observed values of $d\epsilon_\theta^P/d\epsilon_r^P$ correspond to $\sigma_\theta^*/\sigma_r^*$ of 1.03 and 1.08 respectively which means that σ_θ^* and σ_r^* differ at most by about eight percent. If the flow rule is applied to Equation (1.4) and the results are evaluated for $\sigma_\theta = 2\sigma_z$, that is pure internal pressure, it turns out that $d\epsilon_z^P$ is equal to zero. This was verified in test MPP12-L2 in which ϵ_z^P did not exceed 100 micro inches per inch for values of ϵ_θ^P in the range of 1500 micro inches per inch.

Since the assumed anisotropy is based on the fact that observed states of stress at yielding in pure internal pressure are greater than would be predicted by isotropic theory, it is of essential importance to know whether the stress values were determined correctly. The question then is whether the stresses computed from thin-walled tube theory are correct. To check this point, an analysis was performed for a thick-walled tube made of a material which is elastic before yielding and is linearly kinematic hardening after yielding. The analysis is an extension of material discussed by Hill.[4] For the Tresca yield criterion, the internal pressure which causes yielding to occur at the outer surface is

$$p_o = \sigma_o \ln\frac{b}{a} - \frac{\sigma_o\left(\frac{3c}{2E}\right)}{\left(1+\frac{3c}{2E}\right)}\left[\frac{1}{2}\left(1-\frac{b^2}{a^2}\right) + \ln\frac{b}{a}\right] \qquad (1.9)$$

where

σ_o = yield stress
b = outer radius of tube
a = inner radius of tube
c = strain hardening coefficient
E = Young's modulus.

Initiation of yield at the outer surface, rather than the inner surface, is pertinent since strains must be measured on the outer surface and the outer surface strains remain elastic until yielding has proceeded to that region. For dimensions characteristic of the molybdenum tubes, namely a = 0.250-inch and b = 0.280-inch, the pressure at yielding from Equation (1.9) is $p_o = 0.1193\sigma_o$. This must be compared to the pressure at yielding from the second of Eqautions (1.1). That is

$$p_o = \frac{\sigma_o t}{r} \qquad (1.10)$$

where

$$t = b - a$$

$$r = \frac{1}{2}(a+b) \quad .$$

In this thin tube case, $p_o = 0.1132\sigma_o$. Thus the error in using the thin tube approximation appears to be less than six percent.

With anisotropy of the initial yield condition reasonably well established, it is then of interest to consider which of Equations (1.3), (1.4), or (1.5) appears to be in best agreement with experiment. In Figure 7 the only one of the three criteria which can be made to pass through the points on the σ_z-axis and on $\sigma_\theta = 2\sigma_z$ and be in even approximate agreement with points for MPP-4 and MPP-3 is an anisotropic maximum reduced stress figure. A possible form of maximum reduced stress in which $\sigma_\theta^* = \sigma_r^*$ and both are greater than σ_z^* is sketched on Figure 7.

Figures 8 and 9 give test results in which loading was along a side of the yield surface. In Figure 8, the loading was in pure tension to a stress well above the yield stress in pure tension. At that point the tensile load was held constant and internal pressure was increased so that the stress path followed the line shown from top to bottom. According to kinematic hardening theory, the plastic strain increment vectors should be perpendicular to the yield surface at the point where it is contacted by the stress point. It should be noted that the plastic strain increment vectors (arrows on figure) are all parallel for this loading indicating that the point representing the current state of stress is continually in contact with a flat side. Further the plastic strain increment vectors are not perpendicular to the loading path thus demonstrating that the side of the yield surface mades a slight angle with the loading path. Since, in this region of the octahedral plane, the side of the maximum reduced stress yield surface is perpendicular to the σ_z-axis or along the loading path shown, then it is apparent that this yield condition is not exactly in agreement with observed experimental results.

Figure 9 gives results for an initial pure internal pressure loading to a state of stress well beyond yield followed by the addition of a tensile axial loading with internal pressure held constant. The loading path is then along the line indicated proceeding from right to left. Here the axial load jumped initially so that the first point on the combined loading path at which data could be taken was the point indicated by the figure 1. From that point

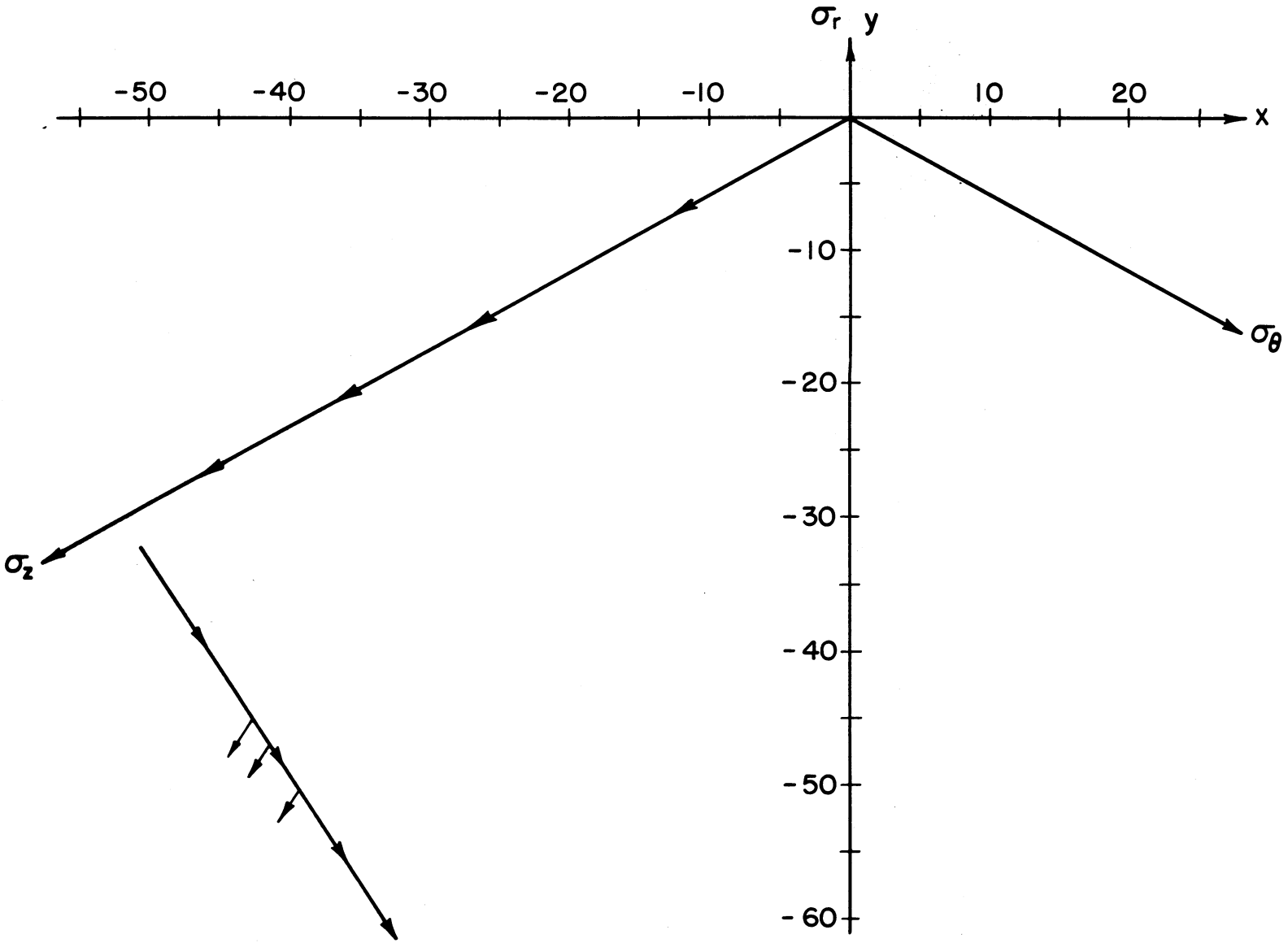

Figure 8. Loading Along Side of Yield Surface. MPP2-L1

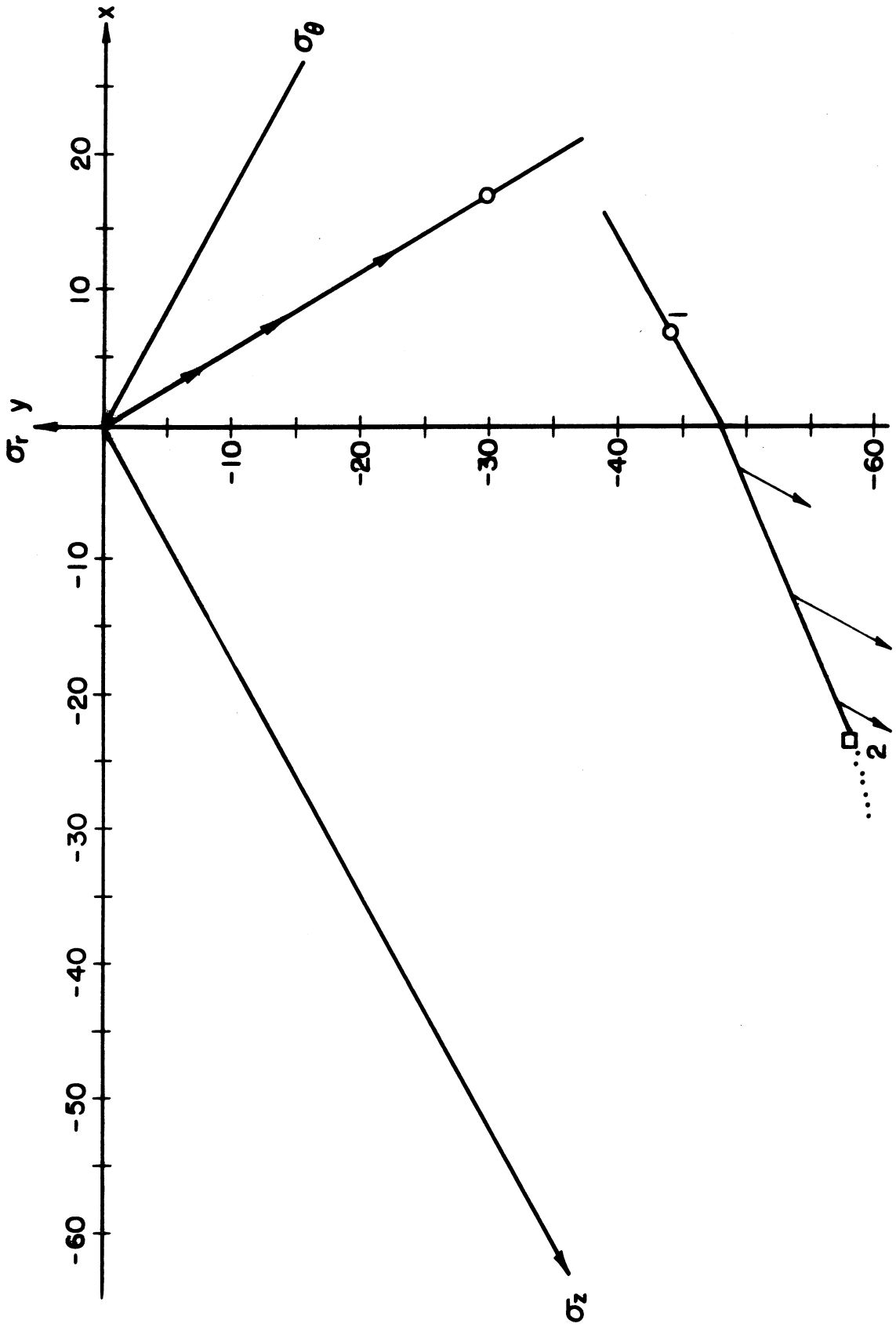

Figure 9. Loading Along Side of Yield Surface. MPP-8

to the point indicated by the figure 2, the direction of the plastic strain increment vector was constant. After the latter point, the plastic strain increment vector changed direction to become more closely parallel to the σ_z-axis. Again the indication is that the stress point is in contact with a plane side between points 1 and 2 and that the side is not the same as the loading path. In this region of the octahedral plane, the side of the maximum reduced stress yield surface is perpendicular to the y-axis and plastic strain increment vectors for stress points contacting the yield surface should be in the negative y-direction. Clearly the agreement with experimental results is not perfect. However, point 2 at which the plastic strain increment vector changes direction corresponds approximately to the point at which the stress path would reach the corner of the moving yield surface. Kinematic hardening theory predicts that the yield surface moves as a rigid body in stress space in the direction of the normal to the yield surface at the point where it is contacted by an outward moving stress point. Plastic straining is said to continue as long as the stress point tends to cause outward motion of the yield surface.

To summarize, it appears that the initial yield data are in fairly good agreement with the maximum reduced stress yield criterion if axially symmetric anisotropy is accounted for. However, some other data indicate that the actual yield surface may differ somewhat in form from that characteristic of the maximum reduced stress yield criterion.

B. STRAIN HARDENING

In this investigation, the kinematic theory of strain hardening was used exclusively as a basis for interpreting the experimental data. The test program was planned in such a way that the results could be compared with this theoretical model. The kinematic hardening theory which is due to Prager,[5] is discussed in detail in WADD-TR-869, Part II[1] but for convenience the basic features will be reviewed here. The theory states that the initial yield surface

$$F(\sigma_{ij}) = k^2 \qquad (1.11)$$

becomes, after strain hardening,

$$F(\sigma_{ij}-\alpha_{ij}) = k^2 \quad . \qquad (1.12)$$

The flow rule, Equation (1.6), is assumed to apply and the yield surface is assumed to translate without changing the form of $F(\sigma_{ij})$. The tensor α_{ij} rep-

resents the translation of the yield surface in stress space, the translation occurring in the direction of $d\epsilon_{ij}^P$ (i.e., the outward drawn normal to the yield surface). Thus

$$d\alpha_{ij} = c d\epsilon_{ij}^P \quad . \tag{1.13}$$

Using the condition that the stress point must remain on the translating yield surface, the flow rule, and Equation (1.13) we obtain the following flow law:

$$d\epsilon_{ij}^P = \frac{1}{c} \cdot \frac{1}{\frac{\partial F}{\partial \sigma_{mn}} \frac{\partial F}{\partial \sigma_{mn}}} \cdot \frac{\partial F}{\partial \sigma_{ij}} \cdot \frac{\partial F}{\partial \sigma_{kl}} d\sigma_{kl} \quad . \tag{1.14}$$

where c is the strain hardening coefficient. In view of the preceding discussion, $F(\sigma_{ij})$ will be taken as the maximum reduced stress yield condition, Equation (1.5). After strain hardening, this yield condition becomes

$$\begin{aligned} |\sigma_z - \sigma - c\epsilon_z^p| &= \frac{2}{3}\sigma_z^* \\ |\sigma_r - \sigma - c\epsilon_r^p| &= \frac{2}{3}\sigma_\theta^* \\ |\sigma_\theta - |-c\epsilon_\theta^p| &= \frac{2}{3}\sigma_\theta^* \quad . \end{aligned} \tag{1.15}$$

To obtain Equations (1.15), it is necessary to note that the material is assumed to be incompressible in the plastic range so that

$$d\epsilon_z^P + d\epsilon_\theta^P + d\epsilon_r^P = 0 \quad . \tag{1.16}$$

The flow laws for a stress point on the side of the yield surface perpendicular to the σ_z-axis, for which the first of (1.5) applies, are

$$\begin{aligned} d\epsilon_z^P &= \frac{1}{3c}(2d\sigma_z - d\sigma_\theta - d\sigma_r) \\ d\epsilon_\theta^P &= -\frac{1}{6c}(2d\sigma_z - d\sigma_\theta - d\sigma_r) = d\epsilon_r^P \quad . \end{aligned} \tag{1.17}$$

Similarly the flow laws for the side described by the second of (1.5), i.e., the side perpendicular to the y-axis, are

$$d\epsilon_r^P = -\frac{1}{3c}(2d\sigma_r - d\sigma_z - d\sigma_\theta)$$

$$d\epsilon_\theta^P = \frac{1}{6c}(2d\sigma_r - d\sigma_z - d\sigma_\theta) = d\epsilon_z^P \quad . \tag{1.18}$$

Equations (1.17) and (1.18) or more generally Equation (1.14) represent a linear relationship between the plastic strain increment and the stress increment. For yield conditions such as the maximum reduced stress condition which consist of plane sides in principal stress space, the flow laws can be integrated and thus lead to a linear relationship between plastic strain and stress. Inspection of Figures 3 and 4 indicates that a linear relation between stress and strain (elastic plus plastic) is valid as an approximation only for a limited range of stress above the yield stress. Thus the computation of total plastic strains by integrating Equations (1.17) or (1.18) would not be expected to be in agreement with experimental values for molybdenum if the stresses are greatly in excess of the yield stress. A better model for molybdenum would be a bi-linear material in which one value of the strain hardening coefficient applied for stress states from yield up to a selected state of stress and then a smaller value of the strain hardening coefficient applied thereafter. This would, however, compound the difficulties in solving boundary value problems.

In the kinematic theory of strain hardening it is assumed that after unloading from a state of stress that has caused plastic straining and motion of the yield surface, further plastic strain does not take place until the translated yield surface is again contacted at some point. More simply, if a specimen is loaded in pure tension to a point beyond initial yield, then unloaded, and finally reloaded, yielding on reloading should occur at a stress equal to the maximum stress reached previously. However, in Figure 5 it appears that the proportional limit stress for loading L5 is notably less than the maximum stress reached on the previous loading. For the other loadings the theory is followed rather well. Similar results are given in Figure 6 for pure internal pressure loading. Here the proportional limit stress in the last loading is less than the maximum stress reached during L9. For other loadings the proportional limit stress is approximately equal to the maximum stress previously reached. From this it is concluded that for stresses well beyond the initial yield stress or equivalently for large translations of the yield surface, yielding on reloading in the same sense will occur before the yield surface is reached.

The investigation of plastic behavior under combined loadings and for multiple stress paths provides the most general test of theory and gives the

most information on material behavior. Results from such experiments plotted in the octahedral plane of principal stress space follow. In all cases, the maximum reduced stress criterion of yielding is assumed to apply. For each set of data the yield surface is made to pass through two initial yield points which locate adjacent sides of the surface. Inconsistency from specimen to specimen precludes the use of the same size of yield surface for all cases.

In Figure 10 data from test MPP-7 are presented. Here the first loading was internal pressure alone with yielding observed at point 1. This loading was continued until the yield surface had been moved to the position indicated by the single dashes. After unloading from this point, the specimen was reloaded in pure tension to yield at point 2. This point lies on both the initial yield surface (solid line) and the first subsequent yield surface (single dashes). Tension loading then continued beyond point 2 and the yield surface moved to the position of the figure formed from the double dashes. This constitutes the second subsequent yield surface. The specimen was then unloaded and reloaded in internal pressure to the point x = 9000, y = -16,000 at which time the pressure was held constant and tensile axial load was applied. In this mode of loading, yielding occurred at the point 3E whereas it should have occurred at point 3T according to the theory. Good agreement of experiment and theory is indicated.

It should be noted that points 1 and 2 are used to define the initial anisotropie yield surface. This is possible even though yield is exceeded during the first loading since the initial stress path is a simple radial one. For pure internal pressure loading the stress point enters a corner of the yield surface and thus during strain hardening the yield surface moves in the direction of the stress increment. Thus the side perpendicular to the σ_z-axis merely moves laterally along its initial position and thus point 2 must lie on both the initial and first subsequent yield surfaces.

Figure 11 illustrates data from another test in which the initial anisotropic yield surface was defined by an initial loading in pure tension followed by pure internal pressure loading. For the initial tensile loading, yield occurred at point 1 and the loading was continued to move the yield surface to the position indicated by the single dashes. Unloading then occurred followed by reloading in internal pressure. Yielding now occurred at point 2. This point must necessarily be on a side perpendicular to the σ_θ-axis. Since the direction and extent of yield surface motion is known from the initial loading, the original position of the side perpendicular to the σ_θ-axis can be determined. Further the initial yield surface has a corner on the line $\sigma_\theta = 2\sigma_z$ so that the side perpendicular to the y-axis can be located. The initial yield surface is represented by a solid line.

Continuing with the data of Figure 11, the internal pressure during second loading was increased beyond point 2 so that yield surface attained the position indicated by the double dashes. After unloading, the third

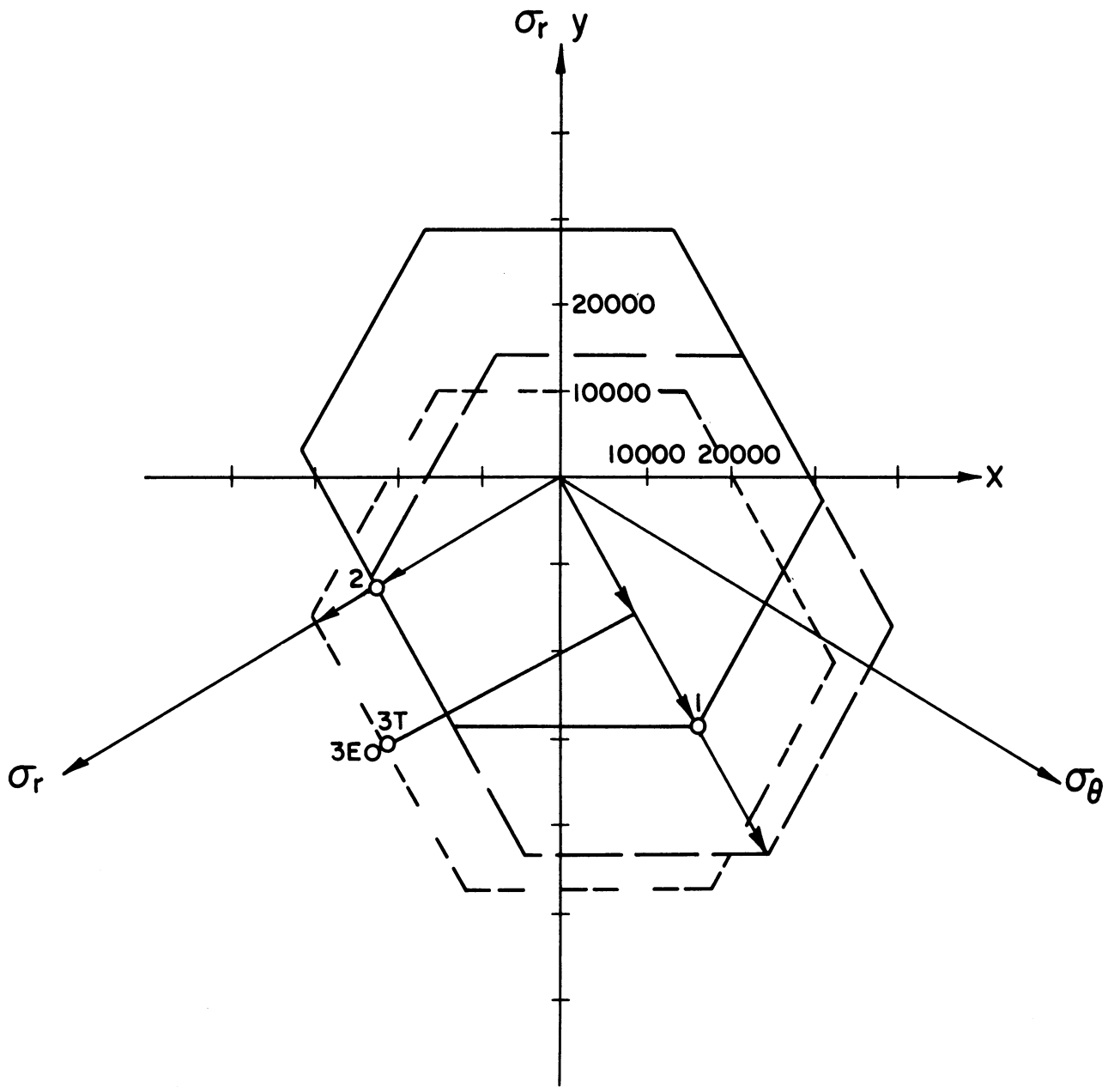

Figure 10. Strain Hardening Behavior. Test MPP-7. 75°F

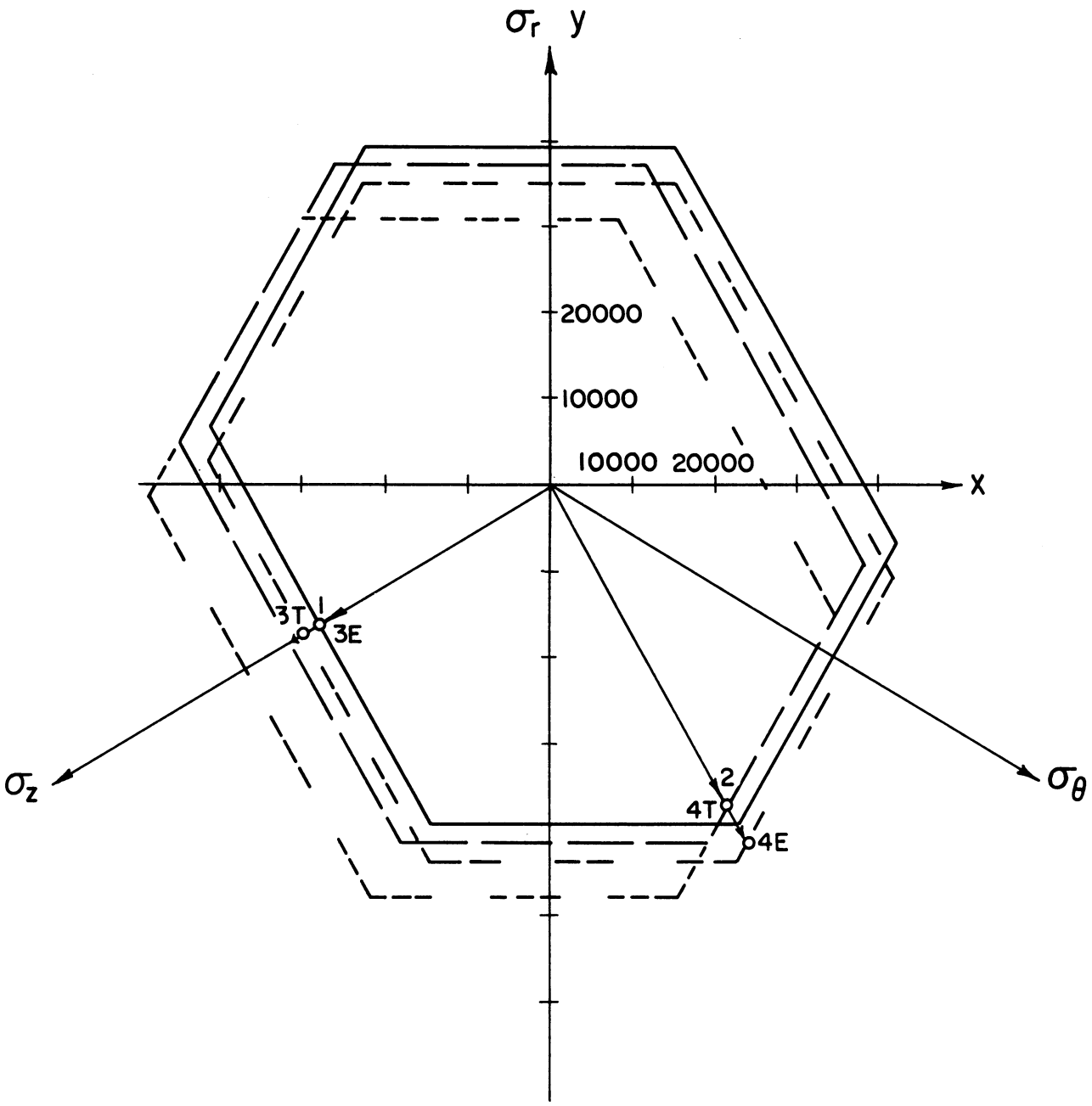

Figure 11. Strain Hardening Behavior. Test MPP-10. 75°F

loading path was again tension to yielding at point 3E. Point 3T would be the yield point predicted by theory. The tension loading continued until the yield surface was moved to the position indicated by the figure composed of triple dashes. Again after unloading, the fourth loading was in internal pressure to yielding at point 4E rather than point 4T as predicted by theory. Points 3E and 4E are in fair agreement with the theory. However, the yield surface motions are quite small and thus scatter in the data may mask the true behavior.

In Figure 12, the initial anisotropic yield surface is defined by an initial loading in internal pressure and a second loading in tension. The points 1 and 2 then fix the initial yield surface. Note that the second loading did not proceed beyond point 2. Here the third loading was a combination of axial force and internal pressure so that $\sigma_z = \sigma_\theta$ approximately. Yielding occurred at point 3T which, in this instance, coincides with point 3E lying on the first subsequent yield surface (single dashes). The fourth and last loading was axial tension in which the material yielded at point 4E rather than point 4T as predicted by theory. However, point 4E does not lie far away from the second subsequent yield surface (double dashes) and, if the downward motion of this surface had been slightly larger, the agreement would be improved. Another interpretation would be that the yield second subsequent yield surface either has decreased in size relative to the initial yield surface or has changed shape. A fifth loading, not shown, in internal pressure showed yield at a stress point well inside the second subsequent yield surface thus lending support to the latter interpretation.

Figure 13 gives data for a specimen in which the yield values are sensibly lower than in other tests. However, the data appear to be acceptable in all other respects. The first loading was in axial tension with yield at point 1 and the first subsequent yield surface given by single dashed lines. Yield occurred during the second loading in internal pressure at point 2 and the yield surface was moved to the position of the second subsequent yield surface (double dashes). In this case the motion of the yield surface is so great that the second subsequent yield surface does not contain the origin. Thus yielding on unloading would be expected. In fact, the material did yield upon unloading at a point estimated to be point 3E. The reliability of point 3E is not good, however, so that the difference between point 3E and the theoretical yield, point 3T, is not thought to be significant. In this case, the unloading from the maximum point in the second loading is treated as the third loading. For the fourth loading, the internal pressure was increased to about 1000 psi and then held constant while axial tension was applied. In this mode, yield occurred at point 4E rather than at point 4T which would be predicted by theory. Point 4T lies on the third subsequent yield surface (triple dashes) which was obtained when the corner of the second subsequent yield was moved back to the origin during third loading (unloading). Agreement here between theory and experiment is good especially in view of the fact that the yield point is difficult to detect

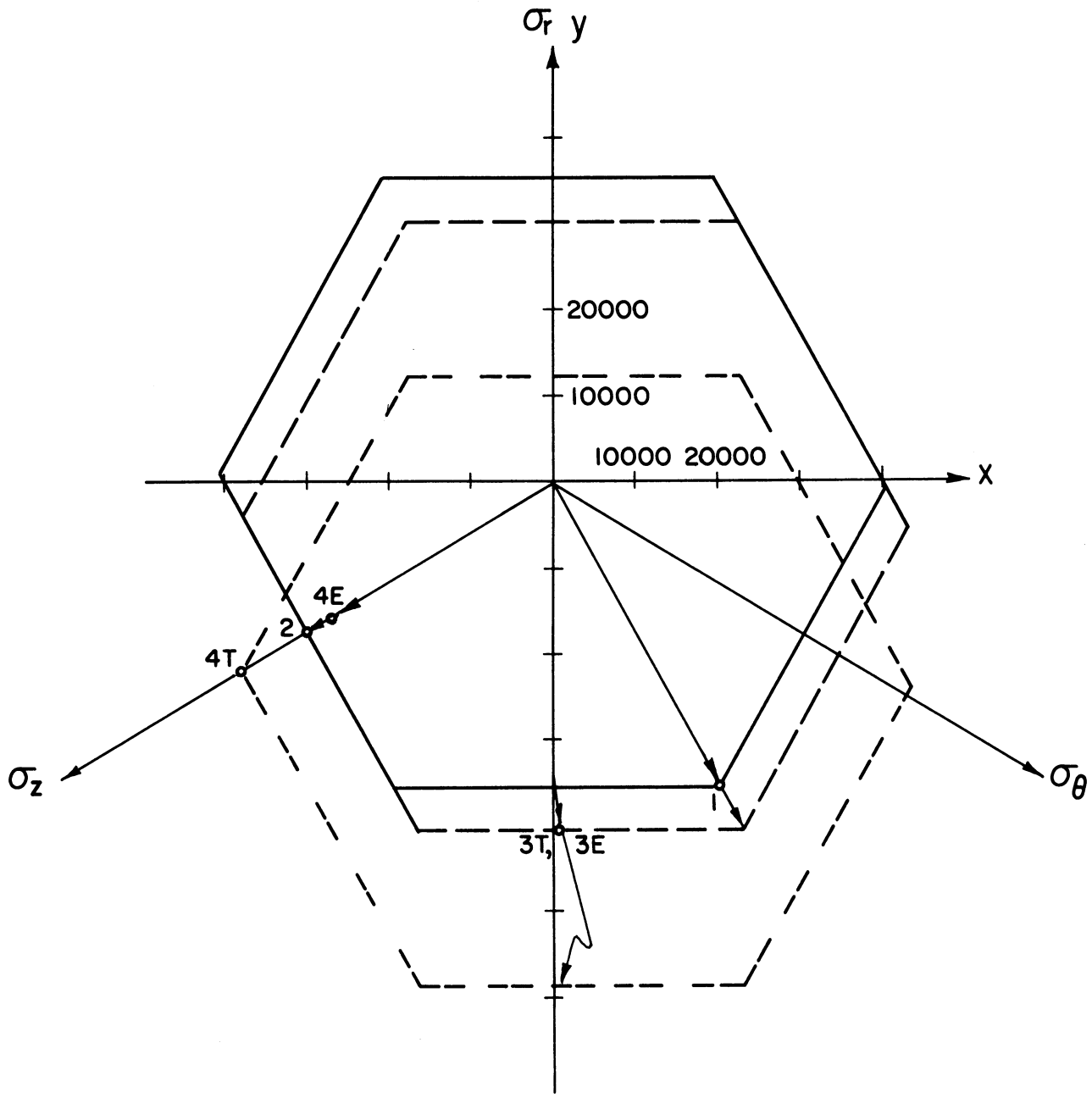

Figure 12. Strain Hardening Behavior. Test MPP-11. 75°F

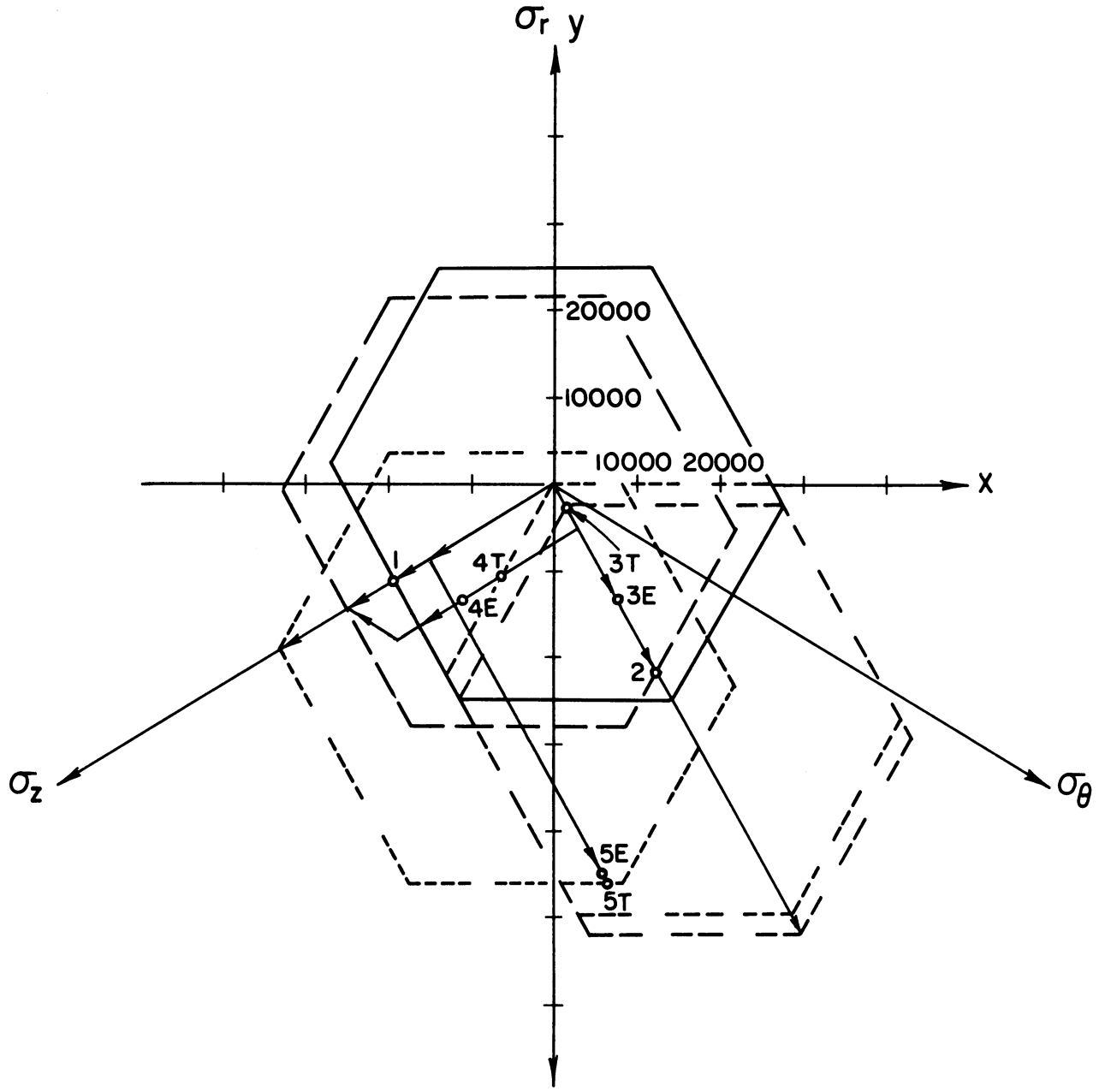

Figure 13. Strain Hardening Behavior. Test MPP-12. 75°F

when the stress path intersects the yield surface at a small acute angle. As can be seen in Figure 13, the internal pressure was eventually reduced to zero during the fourth loading and loading in pure tension continued until the fourth subsequent yield surface (quadruple dashes) was positioned as shown. The fifth loading is also a combined loading consisting of axial tension held at about 1000 pounds with varying internal pressure. Yielding occurred at point 5E, very close to the theoretical point 5T.

In Figure 14, the initial yield surface was established by initial axial tension followed by a second loading in internal pressure. Yielding during the initial loading occurred at point 1 and the yield surface was moved to the position indicated by the single dashed lines, i.e., the first subsequent yield surface. For the second loading, the material yielded at point 2. The second loading was continued past point 2 and the yield surface was moved to the position indicated by the double dashes. The third loading was again pure tension with yield occurring at point 3E. This is in good agreement with the theoretical point 3T lying on the second subsequent yield surface.

The remainder of the strain hardening data were obtained in tests at 212°F. As would be expected, values of stress at initial yield are approximately the same for tests at 75°F and 212°F. However, there appears to be a trend for σ_z^*, the yield stress in the axial direction, to be smaller at 212°F than it is at 75°F while σ_θ^*, the yield stress in the circumferential direction remains the same. To give a quantitative idea of the reduction in σ_z^*, in tests MPP-16, 17, and 18 at 212°F the value of σ_z^* was about 27,500 psi while in tests at 75°F the minimum value of σ_z^* was 35,300 psi with a maximum of 43,100 psi. There appears to be no clear explanation of the reduction of σ_z^* with increasing testing temperature while σ_θ^* remains unchanged.

It should be mentioned that the reason for varying the testing temperature was to influence the fracture behavior rather than the strain hardening behavior.

Figure 15 presents results from a test at 212°F in which the loading pattern is essentially the same as the pattern of Figure 14. As before points 1 and 2 are used to define the initial yield surface (solid line). The first subsequent yield surface is designated by single dashes and the second subsequent yield surface by double dashes. During the third loading, simple tension, yielding occurred at point 3E. Theory predicts yielding at point 3T so that the material yields before the second subsequent yield surface is reached.

In Figure 16, initial loading was again in tension and second loading was pure internal pressure. Yielding at point 1 established a point on the initial yield surface (solid line) and the initial yield surface was pushed to the position of the first subsequent yield surface (single dashes). During second loading, point 2 represents yield. The second loading terminated

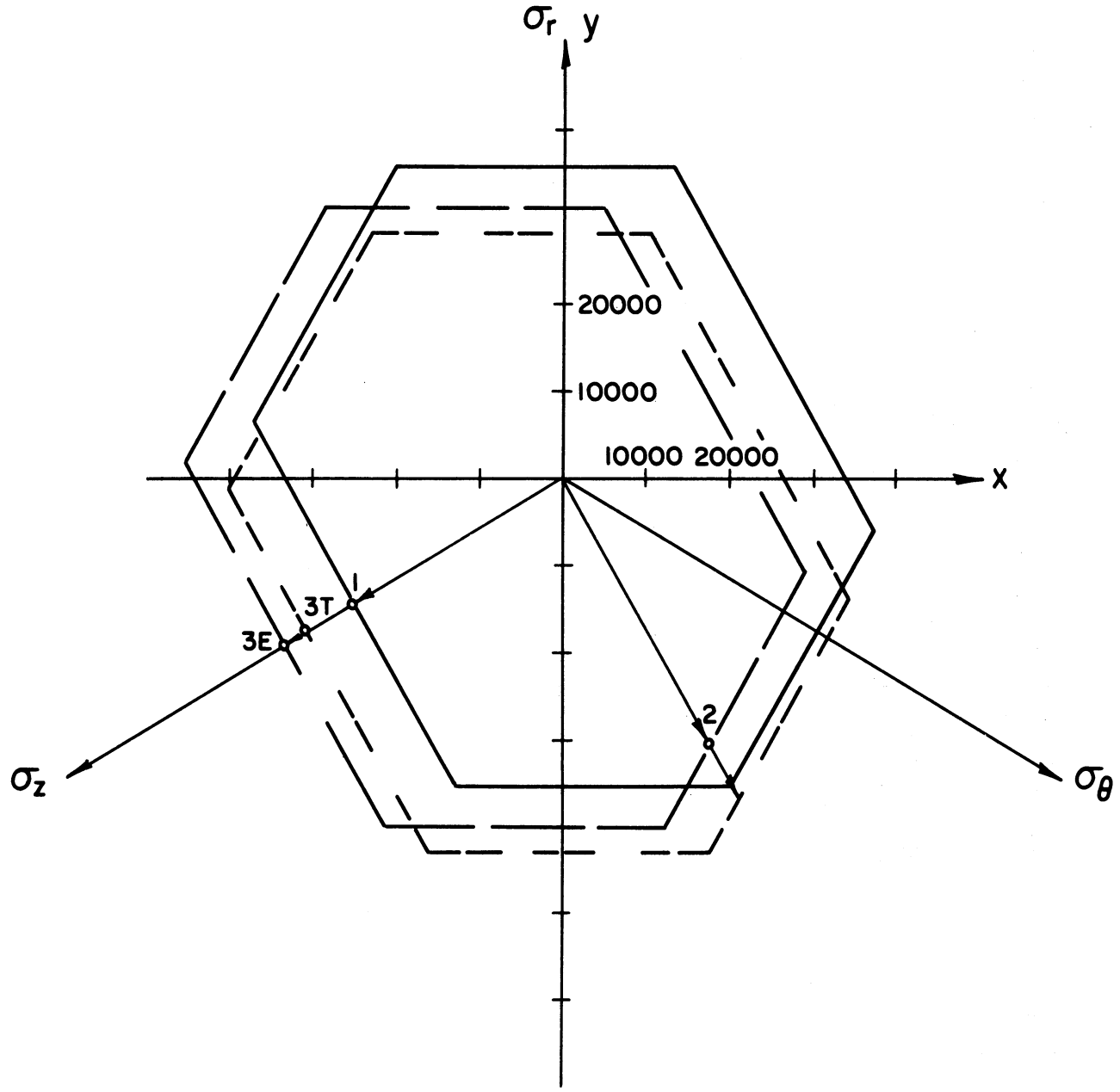

Figure 14. Strain Hardening Behavior. Test MPP-13. 75°F

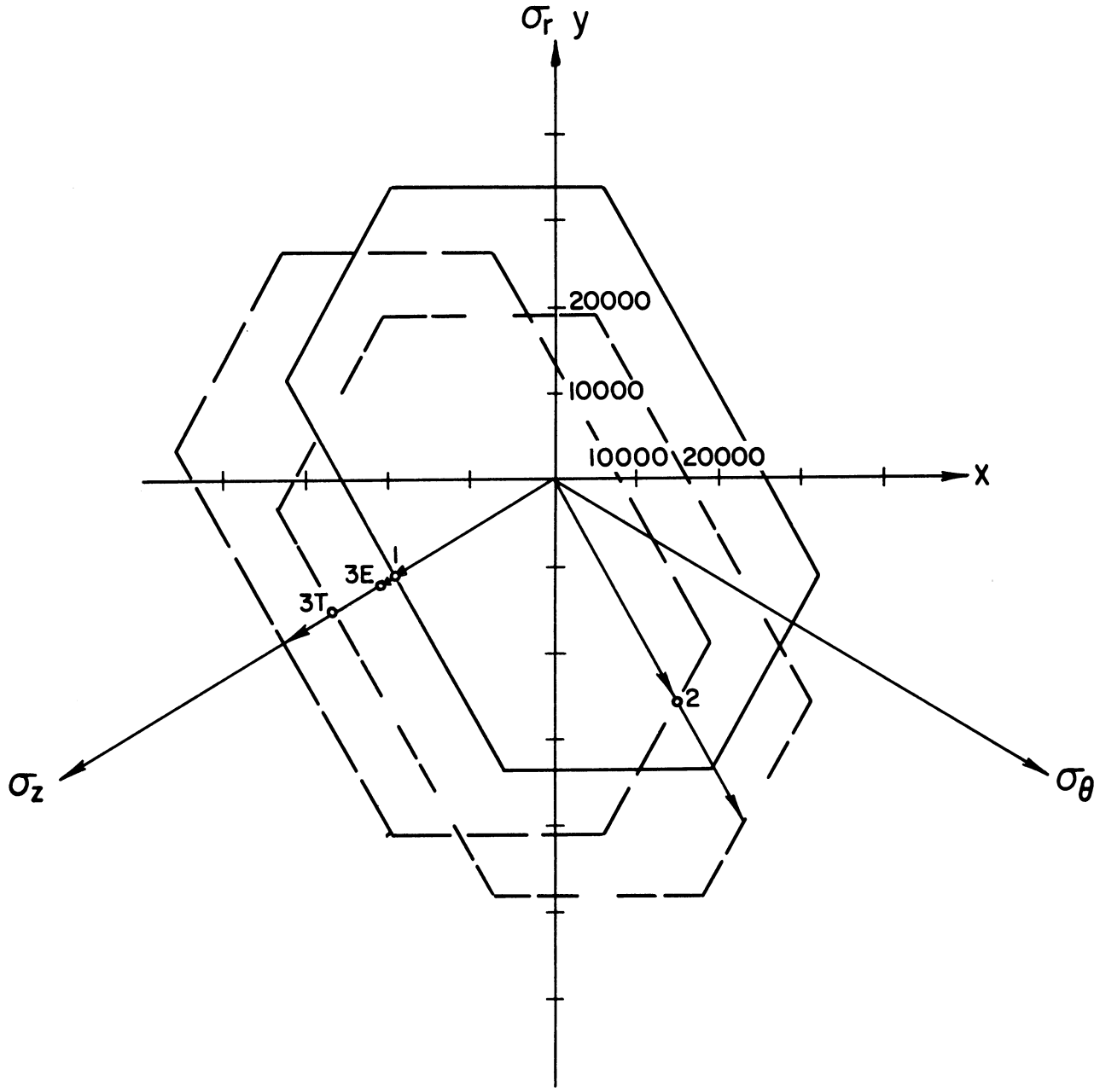

Figure 15. Strain Hardening Behavior. Test MPP-16. 212°F

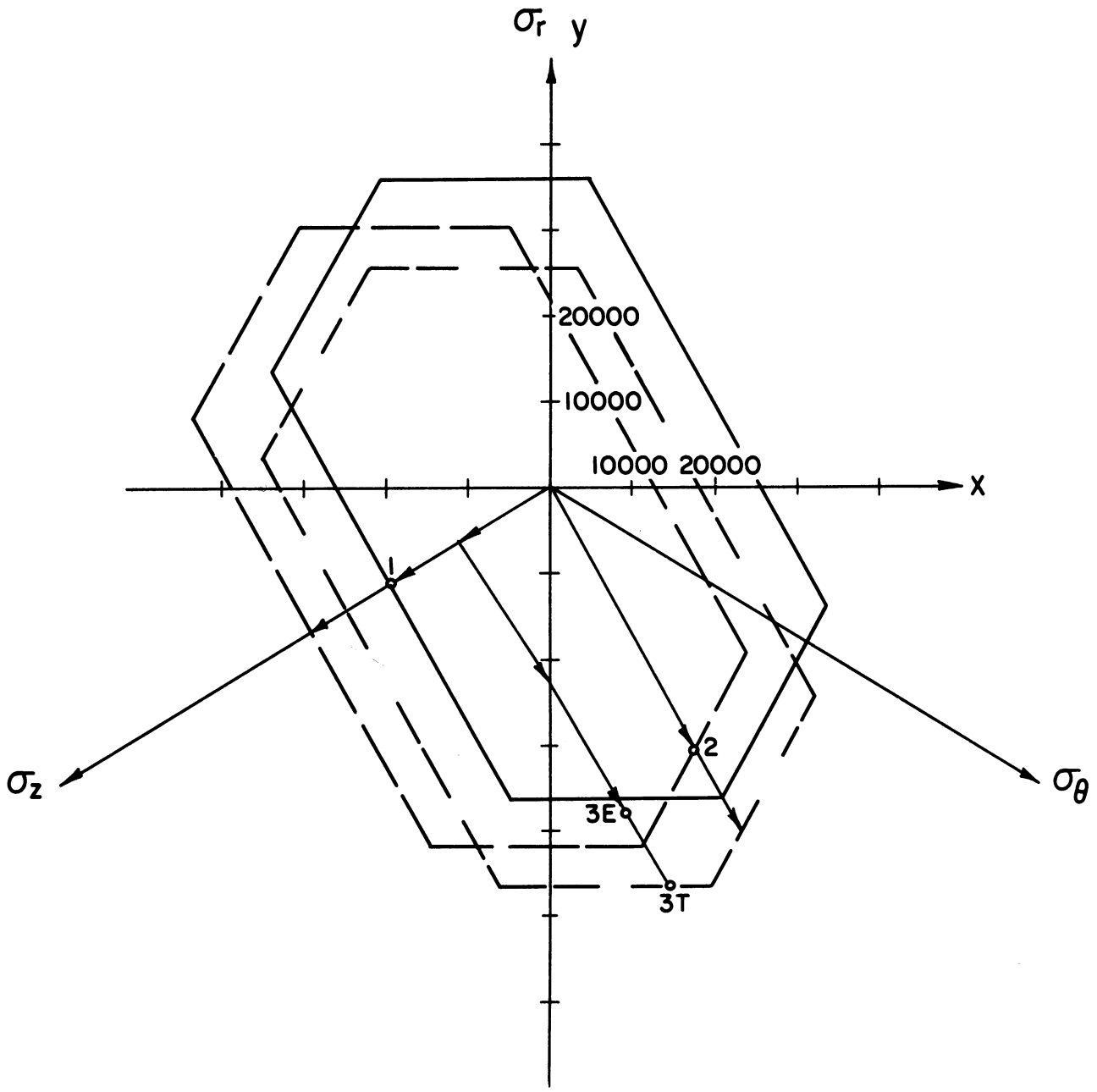

Figure 16. Strain Hardening Behavior. Test MPP-17. 212°F

with the yield surface in the position of the second subsequent yield surface (double dashes). In this test, the third loading consisted of application of axial tension to a point about halfway between the origin and point 1. Then the tension was held constant and internal pressure was added with yield at point 3E rather than at point 3T where the stress path intersects the second subsequent yield surface. As was the case in Figure 15, actual yield occurs before the predicted state of stress is attained.

The test represented in Figure 17 began with a combined initial loading. After loading in tension to x = - 11,000, y = - 6,000, the tension was held constant and internal pressure was applied. The material yielded at point 1 after which loading continued to the position of the first subsequent yield surface (single dashes). The second loading was in axial tension with yield occurring at point 2. Since this point is assumed to lie on the first subsequent yield surface and since the extent of motion of the yield surface is known, another side of the initial yield surface can be located. The extreme point for this mode of loading positions the second subsequent yield surface (double dashes). During the third loading in internal pressure, yielding occurred at point 3E while theory predicts that yielding should occur at point 3T. The third loading finally reached the indicated third subsequent yield surface (triple dashes). A fourth loading consisted of pure tension to a point just past point 2 at which time the tensile load was held constant and internal pressure applied. Note that this loading path lies inside but adjacent to a side of the third subsequent yield surface. In this case, yielding occurred at point 4E and not at point 4T as would be expected from theory. In both third and fourth loadings, the material yields before the appropriate subsequent yield surface is reached.

Figure 18 gives data for a test in which the initial and second loadings are the same as in Figures 15 and 16. As in other figures, the solid line describes the initial yield surface, the single dashes describe the first subsequent yield surface, and the double dashes describe the second subsequent yield surface. For the third loading internal pressure alone was applied to x = 7,000, y = - 11,000. Then the internal pressure was held constant and axial tension was added. Yield occurred at point 3E which is in good agreement with point 3T from theory. To effect the fourth loading, the axial tension was decreased to x = - 14,000, y = - 23,000 when further internal pressure was added with constant tension. Here the material yielded at point 4E which is outside the third subsequent yield surface (triple dashes) on which point 4T lies. This behavior is in contrast to that observed in the previous three figures.

To summarize the data on strain hardening, it was demonstrated first that arc-cast molybdenum is not a linear hardening material so that approximately correct plastic strains can be computed only for a limited range of states of stress above the yield stress. The kinematic theory of hardening, in which the initial yield surface moves as a rigid body in the octahedral

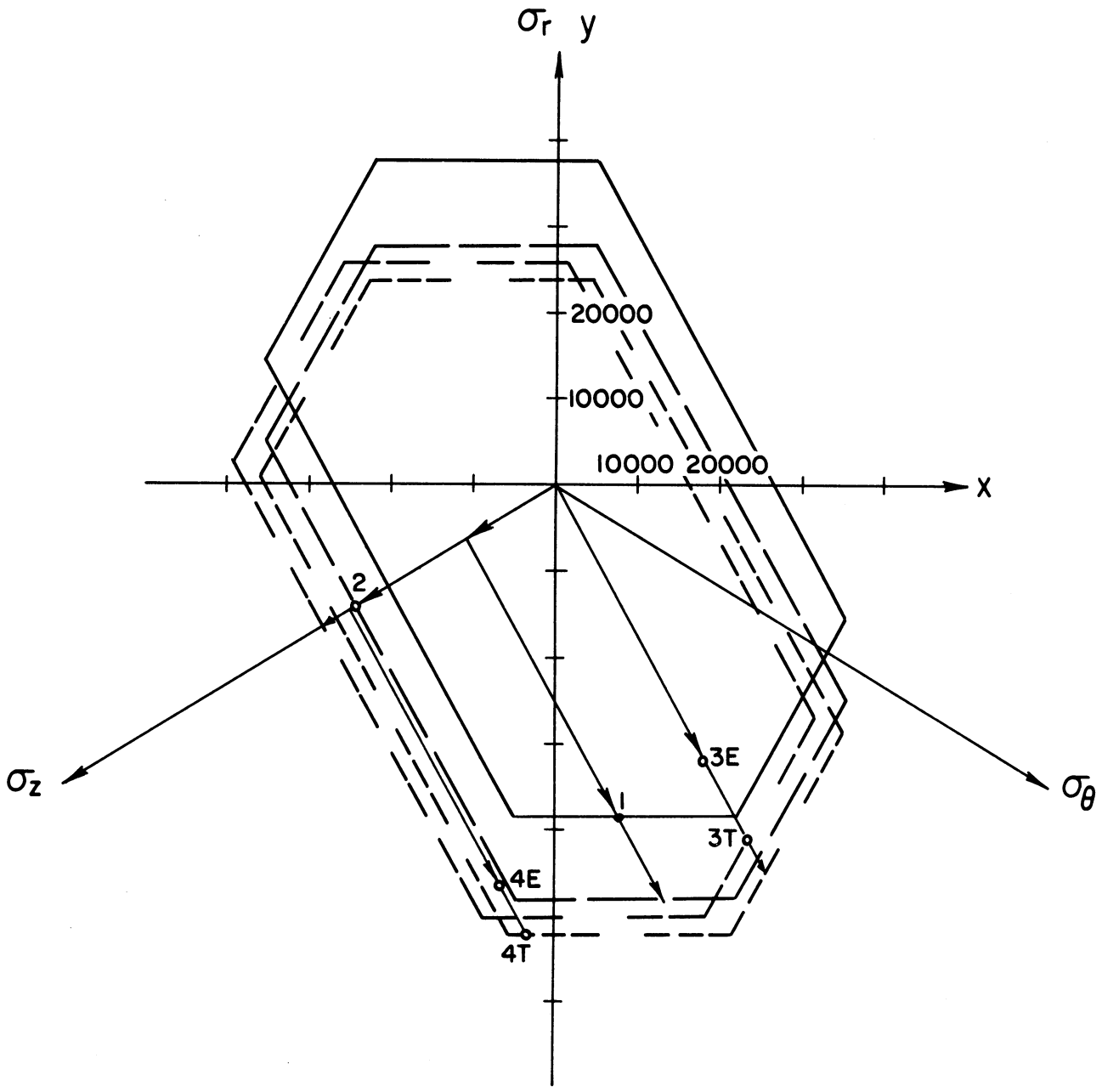

Figure 17. Strain Hardening Behavior. Test MPP-18. 212°F

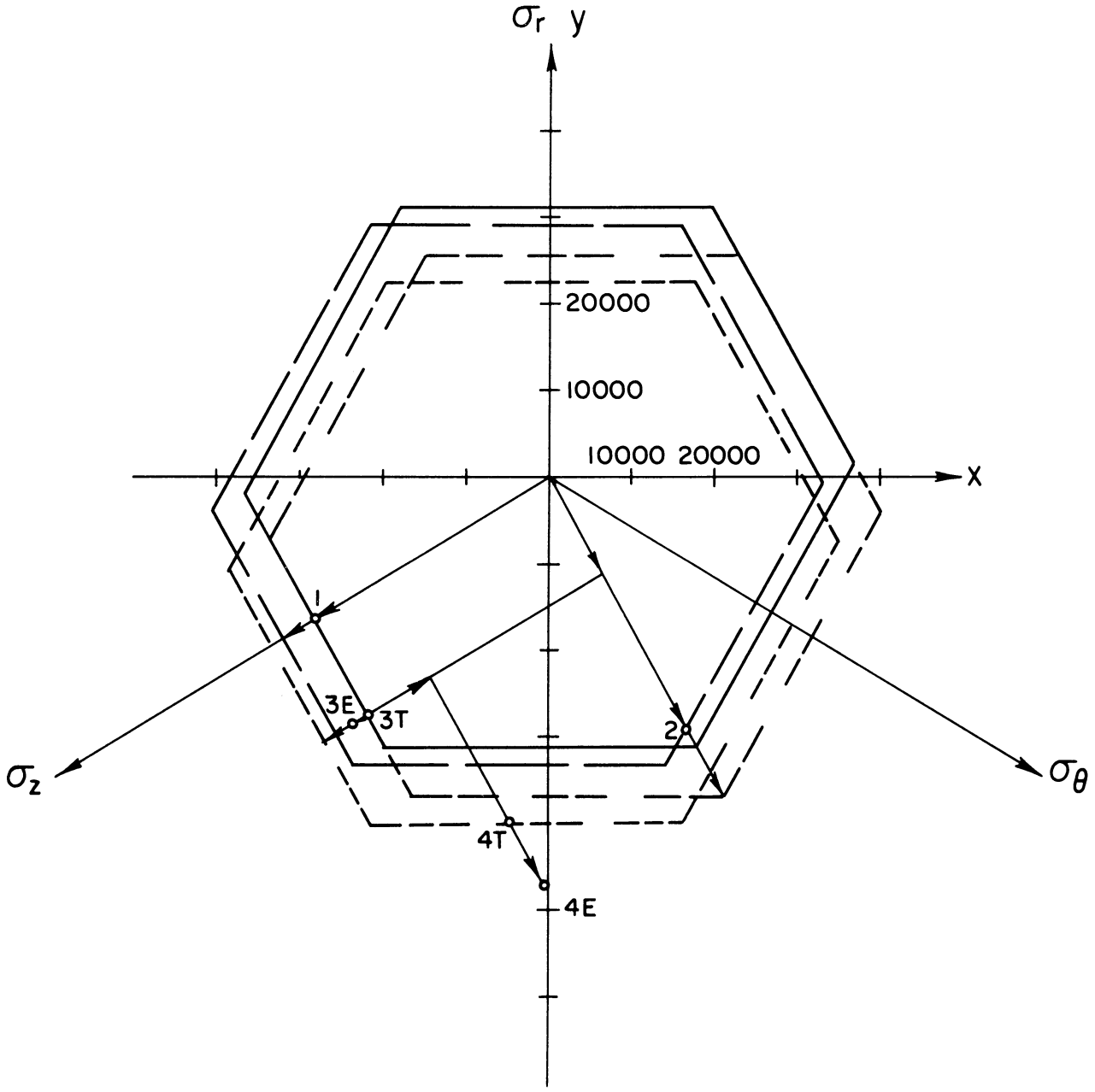

Figure 18. Strain Hardening Behavior. Test MPP-19. 212°F

plane of principal stress space, gave good predictions of the observed behavior of molybdenum at 75°F. In some cases, actual yield points did not lie on or near the fourth subsequent yield surface at 75°F and this may suggest a distortion of the yield surface after extensive plastic straining. For results from tests at 212°F, the kinematic theory of hardening gave markedly poorer predictions of subsequent yield values.

C. FRACTURE

In this research program, fracture stresses in molybdenum tubes were observed at testing temperatures of 75°F and 212°F. The results are compiled in Figure 19 which is a plot of σ_θ^F, the circumferential stress at fracture, versus σ_z^F, the axial stress at fracture. All of these test points represent extremely brittle fracture events except for points lying on or near to the σ_z^F-axis which represent ductile fracture. Points on the σ_z^F-axis are fracture stresses in pure tension. The addition of even small values of circumferential stress appears to cause the mode of fracture to change from ductile to brittle and with increasing circumferential stress the degree of fragmentation during brittle fracture increases. Increasing the test temperature from 75°F to 212°F did not cause much increase in the ductile fracture range in stress space. Even in the ductile fracture case only a slight degree of localization of plastic deformation or necking occurs. To give another measure of ductility, or lack of it, the maximum principal strain at fracture in no case exceeded 0.013 inch per inch.

The principal advantage, in this program, of using a relatively brittle material is that large changes in the specimen geometry do not occur during plastic deformation and thus stresses can be easily computed from Equations (1.1) with the original specimen dimensions. If localized plastic deformation occurs, then simple statically determined stress formulas, such as (1.1), do not apply.

In Figure 19, the solid circles are from tests at 75°F while the open circles are for data at 212°F. Lines drawn in the figure represent a maximum normal stress theory of fracture. For the more extensive data at 75°F, it appears that the fracture stress is also anisotropic since the vertical line corresponds to a fracture stress, σ_r, of 100,000 psi and the horizontal line corresponds to a σ_r of 90,000 psi. It should be noted that the fracture data are not plotted on an octahedral plane of principal stress space because the fracture stress is not independent of the mean stress. The data for 212°F seem to indicate that an isotropic σ_r of 76,000 psi is appropriate.

The concept of a maximum normal stress theory of fracture is a consequence of the Griffith[6] theory for materials of essentially zero ductility. This theory applies to cases of plane stress only and that requirement is satisfied in the thin tubular specimen subjected to axial force and internal

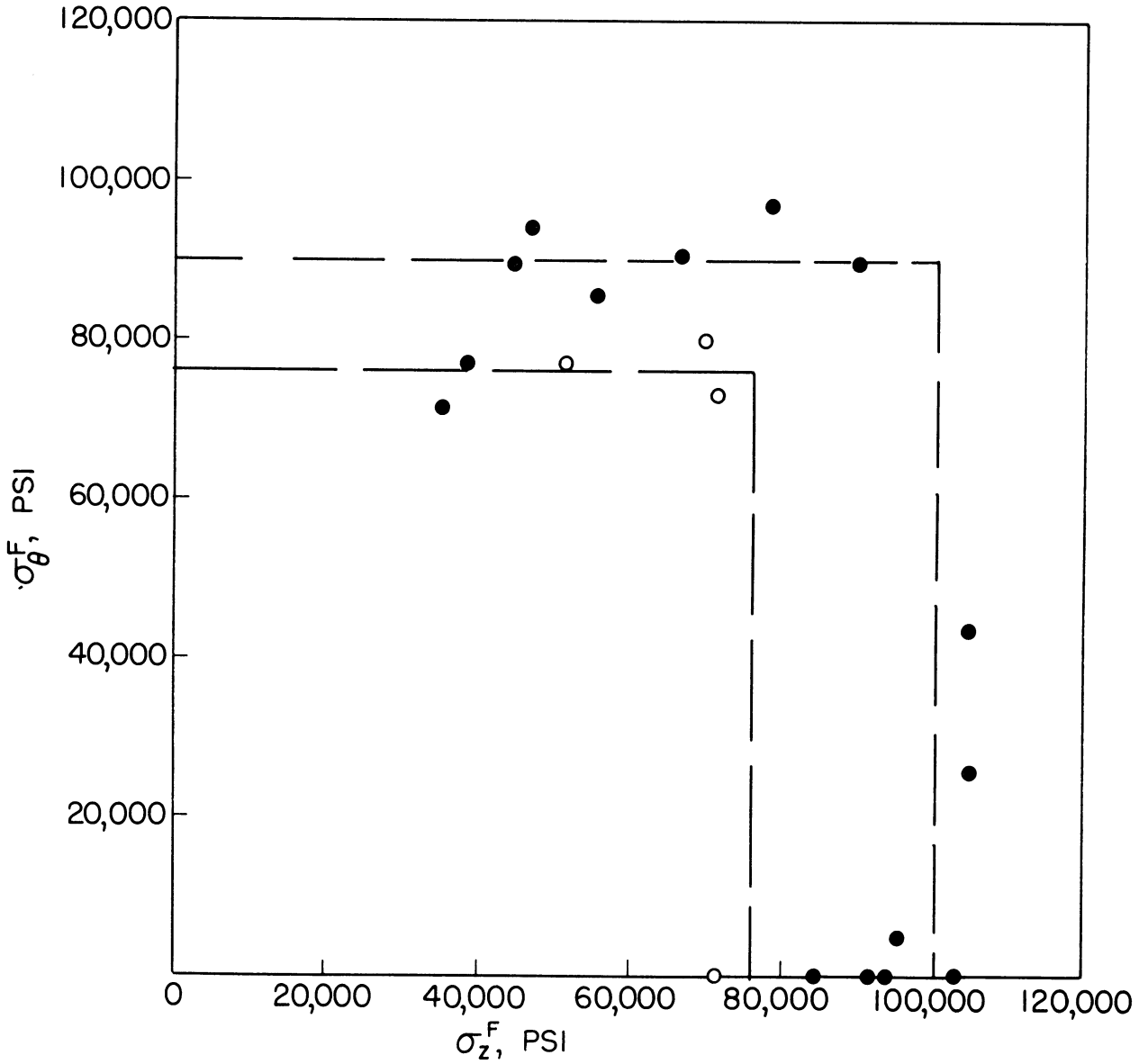

Figure 19. Fracture Data at 75°F and 212°F

pressure. Consider the plane principal stresses to be σ_{max} and σ_{min}. The theory states that, if

$$3\sigma_{max} + \sigma_{min} > 0 \quad , \tag{1.19}$$

then $\sigma_{max} = \sigma_r$. Since both σ_z and σ_θ are positive for tests reported here, then Equation (1.19) is satisfied and the maximum normal stress criterion applies.

Again considering the data for 75°F plotted in Figure 19, the agreement with the maximum normal stress theory of fracture is only fair. However, it is clear that the fracture stress is reduced with increasing test temperature.

PART II

INVESTIGATION OF AN ELASTIC-LINEARLY STRAIN HARDENING BEAM

In this part of the report a theory, in terms of generalized variables, is presented which describes the behavior of a cantilever beam made of a material which is elastic at stresses below the yield stress and, at stresses above the yield stress, is linear strain hardening. The theory is then tested by comparing its predictions with the experimentally observed behavior of cantilever beams of Zamak-3 zinc alloy. This is the same material for which strain hardening data were reported in WADD-TR-60-869, Part II.[1]

A cantilever beam of retangular cross-section with a concentrated force at the free end is considered. Figure 20 is a sketch of the beam.

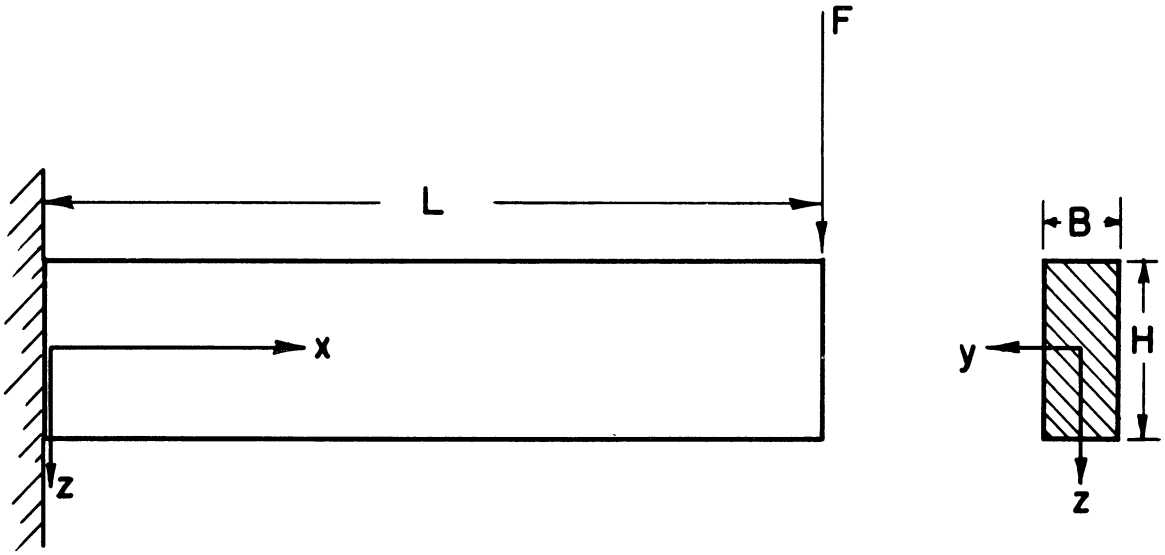

Figure 20. Sketch of Cantilever Beam

It is assumed that beam cross sections remain plane and perpendicular to the beam axis, x, during both elastic and plastic deformation. This implies that shearing strains are negligibly small and that the magnitude of the normal strain is proportional to the distance from the beam axis, i.e., the neutral axis. Thus

$$\epsilon_x = Kz \qquad (2.1)$$

where K is the curvature of the deflected beam axis. If the slope of the beam axis is small then

$$K = -\frac{d^2w}{dz^2} = -w'' \quad . \tag{2.2}$$

Here w is the displacement of the beam axis in the z-direction. Note that K is positive when the beam axis is concave upward.

For purely elastic behavior, we have, by Hooke's Law

$$\sigma_x = E\epsilon_x = EKz \quad , \tag{2.3}$$

the latter by (2.1).

From equilibrium of moments, we obtain

$$M = \int_{-H/2}^{H/2} \sigma_x z dA \quad . \tag{2.4}$$

Equilibrium of axial forces would show that the beam axis passes through the centroid of the beam cross section.

If (2.3) is substituted into (2.4), the following results

$$M = EK \int_{-H/2}^{H/2} z^2 dA = \frac{EBH^3}{12} K = EIK \tag{2.5}$$

in which I is the moment of inertia of a beam cross-section.

For a cantilever, the bending moment, M, at a cross-section which is a distance, x, from the left end, is

$$M = -F(L-x) \quad . \tag{2.6}$$

In view of (2.5), (2.6), and (2.2), the moment-curvature expression for purely elastic behavior becomes

$$w'' = \frac{F(L-x)12}{EBH^3} \quad . \tag{2.7}$$

The limit of the purely elastic range is reached when the stress at the outer fiber of the beam reaches the yield stress, σ_o. If (2.3) is substituted into (2.5) we find

$$M_e = \frac{\sigma_o B H^2}{6} = \sigma_o \frac{2I}{H} \tag{2.8}$$

where M_e represents the maximum elastic bending moment.

After some portion of the material at a given cross section has entered the plastic range of behavior, a new stress-strain law and as a result, a new moment-curvature expression are required. It is assumed that the material follows a linear strain hardening law after the yield stress, σ_o, has been exceeded, and as long as loading continues. For a uniaxial state of stress, this relationship is

$$c\epsilon_x^p = \sigma_x - \sigma_o$$

$$\epsilon_x^e = \frac{\sigma_x}{E} \tag{2.9}$$

$$\epsilon_x = \epsilon_x^e + \epsilon_x^p = \frac{\sigma_x}{E} + \frac{1}{c}(\sigma_x - \sigma_o)$$

where

ϵ_x^p = plastic strain

ϵ_x^e = elastic strain

ϵ_x = total strain

c = strain hardening coefficient.

The relationship is plotted in Figure 2la. It should be noted that, to obtain a uniaxial state of stress in the beam, it is necessary to assume that the shearing stresses can be ignored.

Since the stress path in principal stress space is a radial or proportional loading path, the directions of the stress increment vector and the plastic strain increment vector coincide at all times and thus integration of the stress increment—plastic strain increment relationship, indicated in the first of (2.9), is valid. Kinematic hardening is assumed although isotropic hardining gives the same result unless unloading is considered. The above statement relative to the coincidence of stress increment and plastic strain increment vectors applies for the Tresca yield criterion

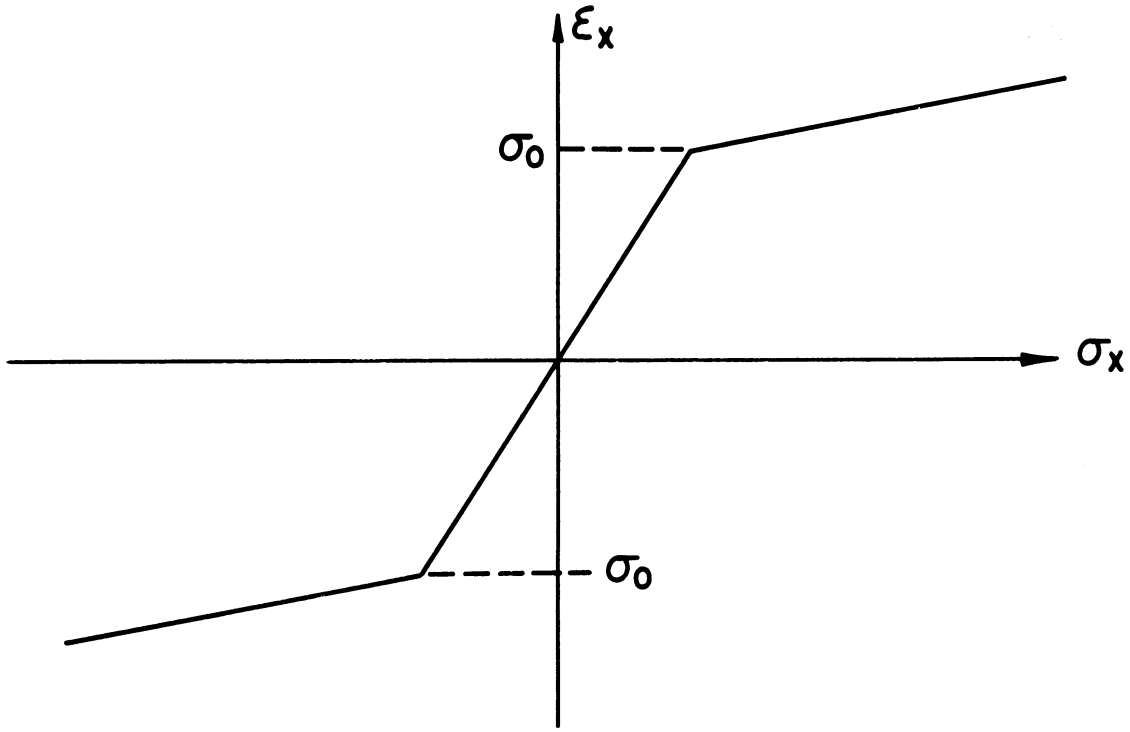

Figure 21a. Elastic-Linear Strain Hardening Stress-Strain Law

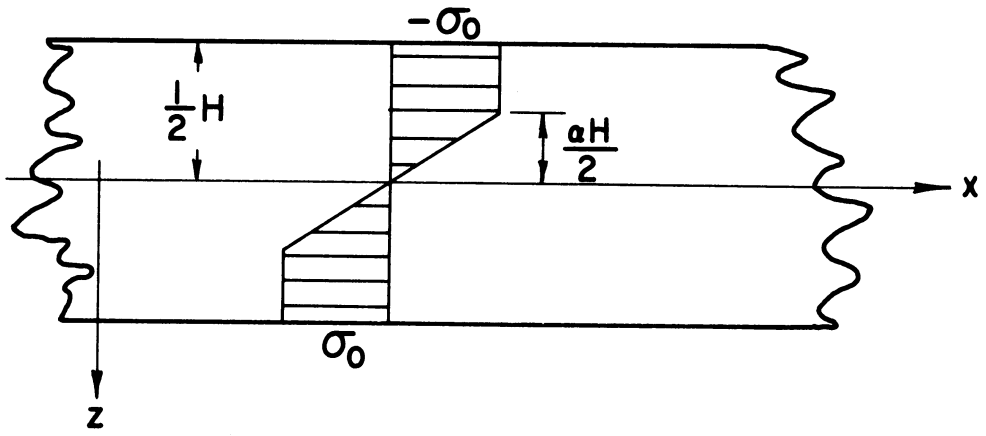

Figure 21b. Stress Distribution at an Elastic-Plastic Cross Section

since the stress path enters a corner. For the von Mises yield criterion this is true for every radial path although the specific relationship (2.9) depends on the shearing stresses being zero. For the maximum reduced stress yield criterion, Equation (2.9) holds even though transverse shearing stress are present.

Since the material is assumed to be incompressible in the plastic range, the assumption of elastic incompressibility is also made.

Now, substitute the last of Equation (2.9) into (2.1) and solve for σ_x to obtain

$$\sigma_x = \frac{Ec}{E+c}\left(Kz + \frac{\sigma_o}{c}\right) \quad . \tag{2.10}$$

At a partially elastic-partially plastic cross section, as shown in Figure 21b, we would expect that Equation (2.10) would apply in the region, $\alpha H/2 \leq |z| \leq H/2$, and that in the elastic region, $0 \leq |z| \leq \alpha H/2$,

$$\sigma_x = \frac{\sigma_o}{\frac{\alpha H}{2}} z \quad . \tag{2.11}$$

Equilibrium of moments then gives

$$M = 2\left[\int_{\alpha H/2}^{H/2} \left(\frac{Ec}{E+c}\right)\left(Kz + \frac{\sigma_o}{c}\right) zBdz + \int_{o}^{\alpha H/2} \sigma_o \frac{2}{\alpha H} z^2 Bdz\right] . \tag{2.12}$$

The curvature is controlled by the elastic core of the cross section so that from Equation (2.3) we find

$$\sigma_o = EK\frac{\alpha H}{2}$$

or

$$\alpha = \frac{2\sigma_o}{EKH} \quad , \tag{2.13}$$

Using (2.13), evaluation of (2.12) gives

$$K^3 + \left[\frac{3\sigma_o}{cH} - \frac{M(c+E)}{cEI}\right] K^2 - \frac{\sigma_o^3}{E^2} \cdot \frac{4}{cH^3} = 0 \quad . \tag{2.14}$$

Now let

$$c = \beta E$$

where

$$0 \leq \beta \leq 1 \quad .$$

Then substitute this along with (2.8) into (2.14) and obtain

$$\left(\frac{K}{K_e}\right)^3 + \left[\frac{3}{2\beta} - \frac{M}{M_e}\left(\frac{\beta+1}{\beta}\right)\right]\left(\frac{K}{K_e}\right)^2 - \frac{1}{2\beta} = 0 \qquad (2.14a)$$

after algebraic manipulation. Note that $K_e = M_e/EI$ is the curvature at the time that the maximum elastic bending moment is reached.

Equation (2.14a) is represented graphically in Figure 22. It can be seen that the cubic moment-curvature relationship for a beam of rectangular cross section becomes linear for values of K/K_e greater than 3. This means, in effect that the last term in (2.14a) can be ignored for the larger values of K/K_e.

If the last term of (2.14a) is completely ignored for all K/K_e, then we have either

$$\frac{K}{K_e} = \frac{M}{M_e}\left(\frac{\beta+1}{\beta}\right) - \frac{3}{2\beta} \qquad (2.15)$$

or $(K/K_e)^2 = 0$ which is a trivial case. Equation (2.15) is an approximate moment-curvature relationship for the plastic range which is linear at all times. In Figure 22, Equation (2.15) can be represented by extending the straight line portions of the curves for $K/K_e > 3$ into the region of smaller K/K_e to the intersection with the elastic moment-curvature line. This intersection occurs at $M/M_e = 1.5$ and $K/K_e = 1.5$.

Hereafter let the approximate relationship be valid throughout the plastic range. This for $0 \leq K/K_e \leq 1.5$, the elastic moment-curvature relationship, (2.5) or (2.7) applies and for $K/K_e > 1.5$ the moment-curvature relationship (2.15) applies.

To obtain (2.15) in a form similar to (2.7) for the elastic case, multi-

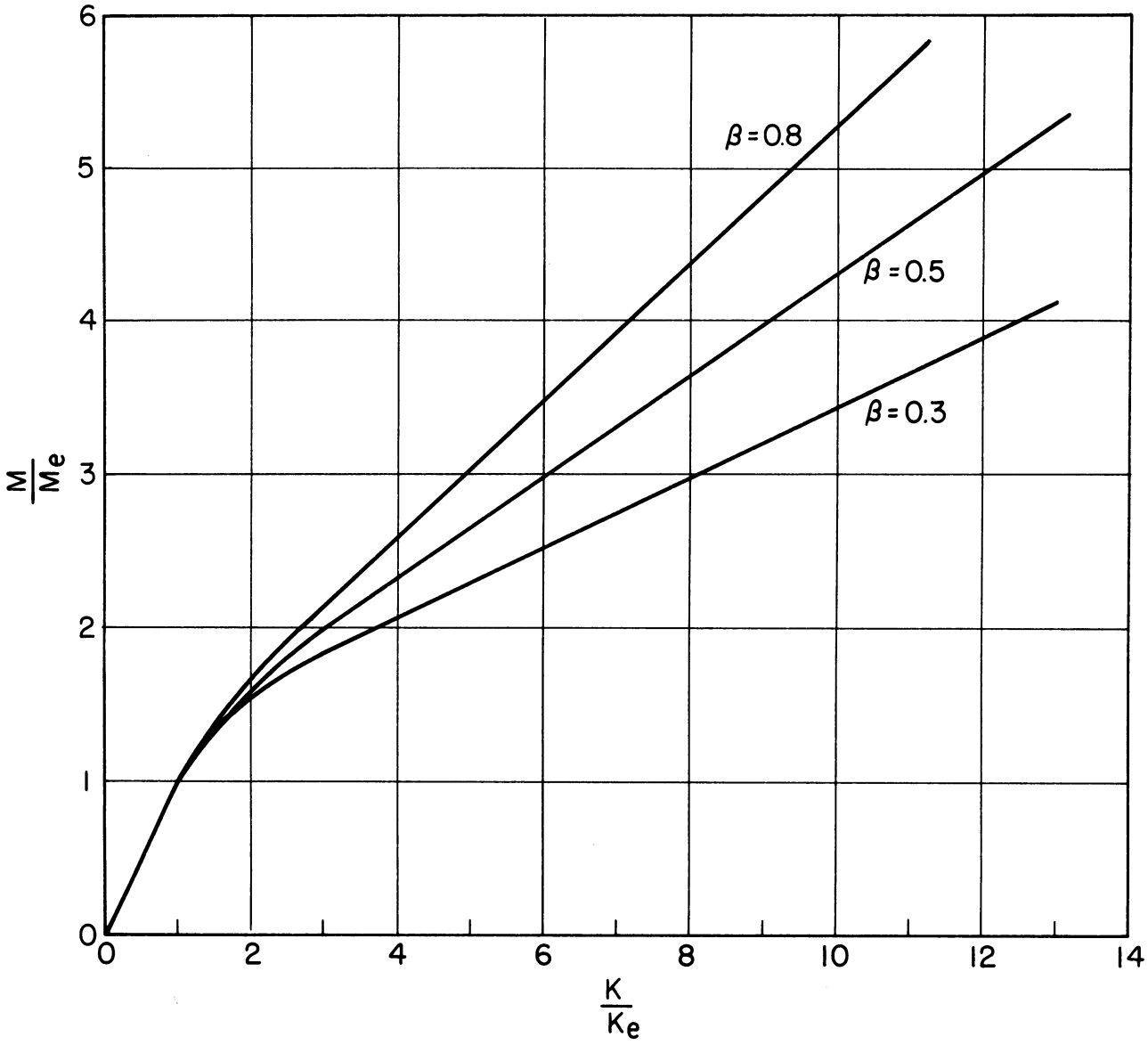

Figure 22. Theoretical Moment-Curvature Relationship for an Elastic-Linear Strain Hardening Beam

ply (2.15) by $K_e = M_e/EI$ and use (2.2) and (2.6). Then

$$w'' = \frac{F(L-x)}{EI}\left(\frac{\beta+1}{\beta}\right) - \frac{3}{2\beta}\frac{F_e L}{EI} . \tag{2.16}$$

In the above, $F_e = -M_e/L$ represents the tip load at which yielding first occurs at the critical cross section.

Equations (2.7) and (2.16) can now be used to compute the tip deflection of the cantilever beam by the so-called "double integration" method. The following conditions must be satisfied

$$\left.\begin{aligned} w &= 0 \\ \frac{dw}{dx} &= 0 \end{aligned}\right\} \text{at } x = 0$$

$$\left.\begin{aligned} w_{left} &= w_{right} \\ \frac{dw}{dx}_{left} &= \frac{dw}{dx}_{right} \end{aligned}\right\} \text{at } x = x_e \quad . \tag{2.17}$$

x_e is the value of x at the boundary between the completely elastic and the elastic-plastic regions of the beam. The last two of Equations (2.17) are continuity conditions at this boundary. Equation (2.16) applies for $0 \leq x \leq x_o$ and Equation (2.7) applies for $x_o \leq x \leq L$.

When the entire beam is elastic or $x_o = 0$ the tip deflection is

$$w = \frac{fF_eL^3}{3EI} \tag{2.18}$$

where $f = F/F_e$. Here, since elastic conditions are assumed to obtain until $K/K_e = 1.5$, f lies in the range $0 \leq f \leq 1.5$.

When some sections of the beam have become elastic-plastic then

$$w = \frac{F_eL^3}{3EI}\left[f + \frac{3f}{\beta}\frac{x_o}{L}\left(1 - \frac{x_o}{L} + \frac{x_o^2}{3L^2}\right) - \frac{9}{2\beta}\frac{x_o}{L}\left(1 - \frac{x_o}{2L}\right)\right] \tag{2.19}$$

and

$$x_o = L\left(1 - \frac{3}{2f}\right) . \tag{2.20}$$

Equations (2.18) and (2.19) are plotted in Figure 23 as F/F_e versus w/w_e where w_e is obtained from (2.18) for $f = 1$.

The predicted load-deflection curves can now be compared with experimental results obtained from tests on cantilever beams made of Zamak-3 zinc alloy. The test pieces were of rectangular cross section having a depth of 3/4 inch and a width of 1/4 inch. The distance from the support to the point of load application was approximately 8 inches. During a test, deflections at the point of load application were measured as well as strains at the upper and lower surface near the fixed end or root. Deflections were read on a dial gage. Loads were applied by a conventional universal testing machine in which loads could be read to the nearest pound.

For Zamak-3, the initial yield stress, σ_o, is about 6000 psi. An elastic load, F_e, of about 20 pounds would result. The theory predicts that a deviation from elastic behavior will occur when the load is 1.5 F_e or about 30 pounds. The slope of the elastic portion of the load deflection curve is expected to be about 590 pounds per foot. This is based on a value of $E = 11.4 \times 10^6$ psi as determined earlier.

Figure 24 gives experimentally determined load-tip deflection and load-root strain curves for one Zamak-3 cantilever beam. In this figure, only the early portion of the loading is shown in order to make clear the point of deviation from elastic behavior. The load-root strain data should deviate from linearity at load F_e since the strain gages were placed near to the fixed end and would thus register yielding in the outer fiber at a cross section very near to the point of maximum moment. It can be seen that the value of F_e appears to be about 23.5 pounds. The plot of load versus tip deflection should deviate from linear or elastic behavior at a load of 1.5 F_e. Examination of Figure 25 shows that the load at deviation is 35 pounds which is 1.49 times the experimental F_e. The slope of the elastic portion of the F-w curve is very near to the predicted value.

Figure 25 presents the entire load-tip deflection curve for the same specimen as above. It is apparent that the linear load-deflection relation, as in Equation (2.19), for the elastic-plastic range is only approximately correct. Up to a load of about 65 pounds or to a tip deflection of about 0.14 inch the approximation is reasonably good. However, only approximate agreement would be expected since the Zamak-3 is not a linear strain hardening material. The stress-strain curve for Zamak-3 has a continuously turning in the plastic range. It is noteworthy, however, that the rather gross assumption of linear strain hardening does give acceptable predictions up to a load which is three times the load at first yielding.

Unloading from a maximum load of 82 pounds is also shown in Figure 25. Initially, unloading is elastic and yielding upon unloading occurs at a load of about 24 pounds. According to kinematic hardening theory yielding during

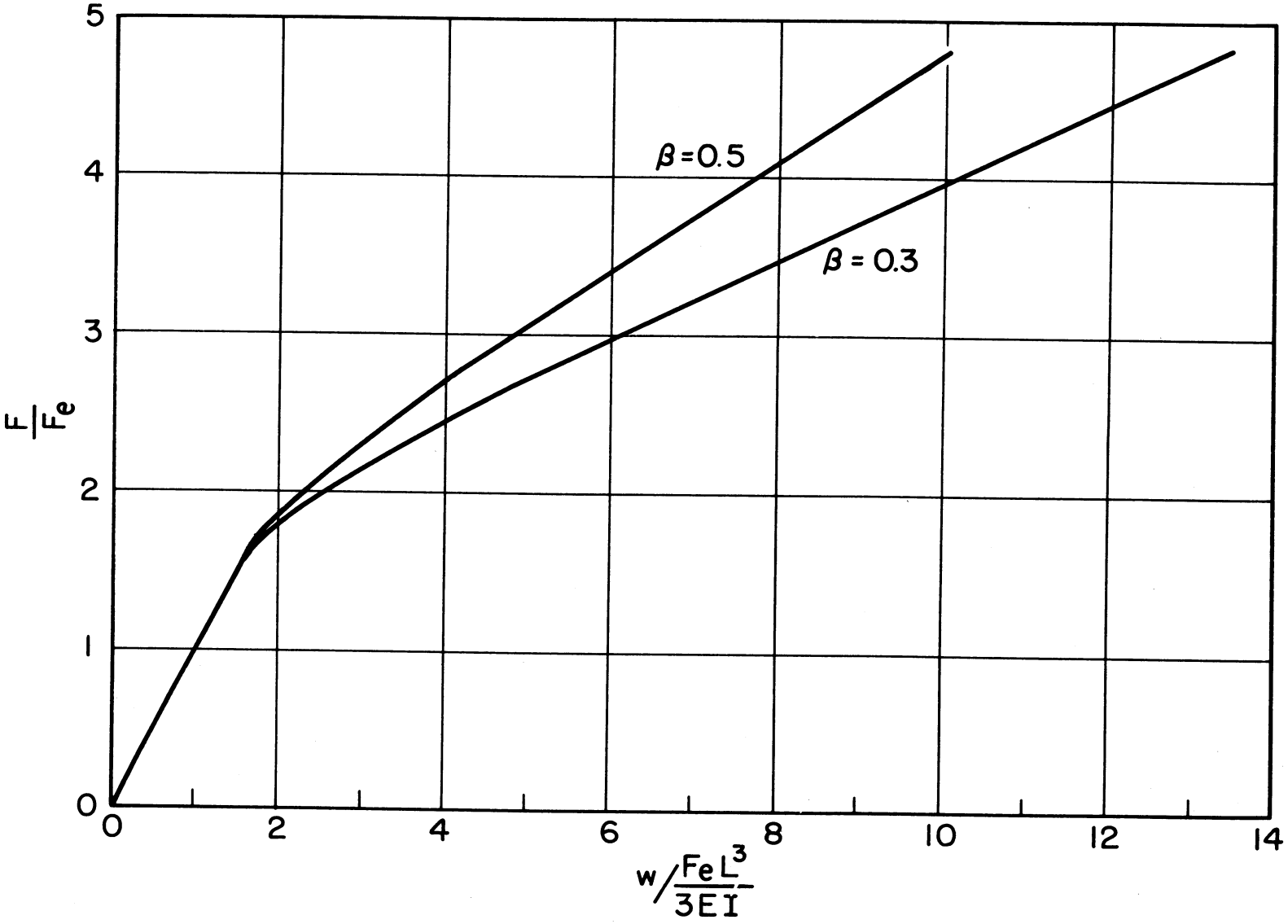

Figure 23. Load versus Tip Deflection for an Elastic-Linear Strain Hardening Beam

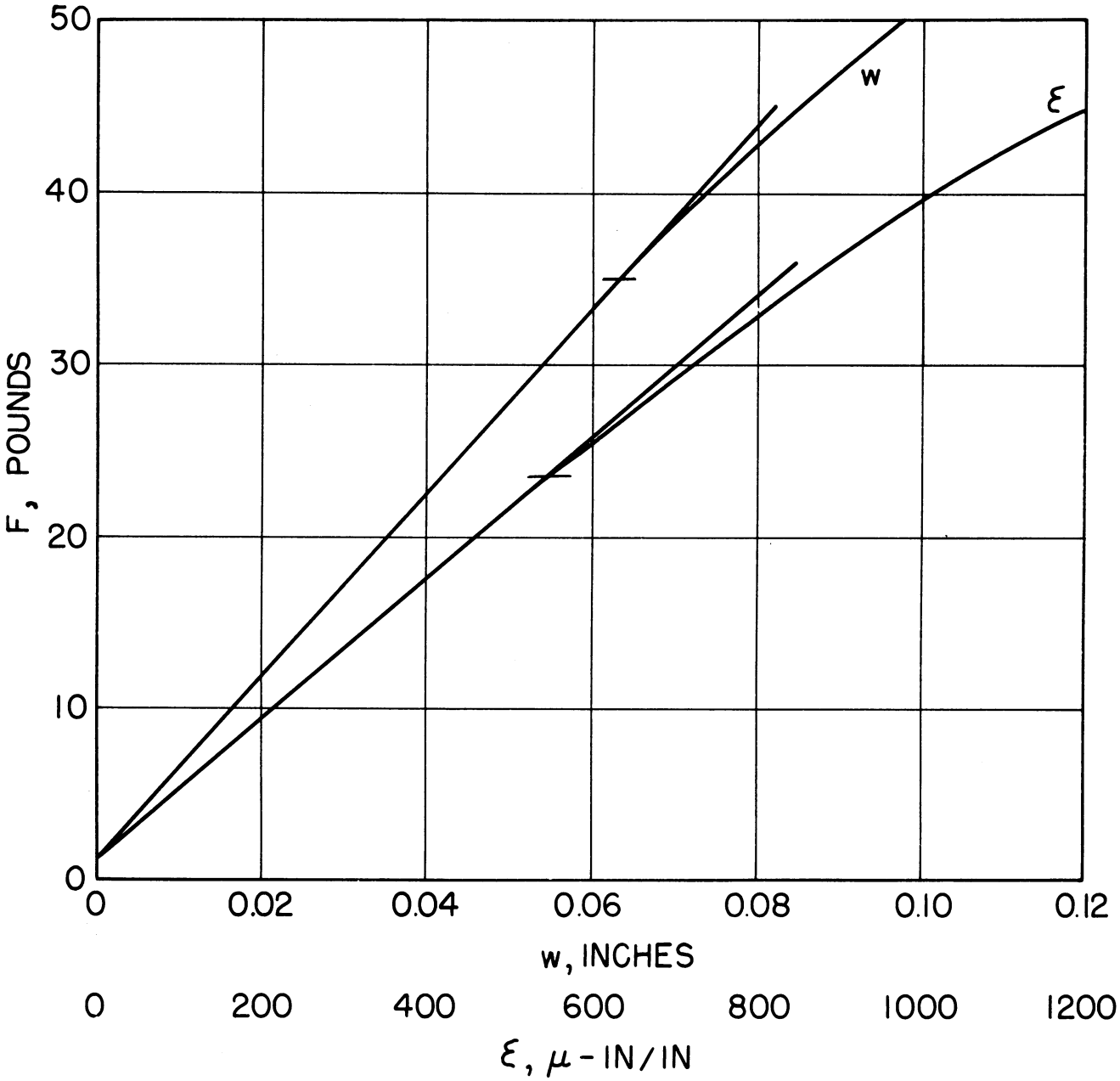

Figure 24. Load-Deflection and Load-Strain Curves for Zamak-3 Cantilever Beam (ZAB-2)

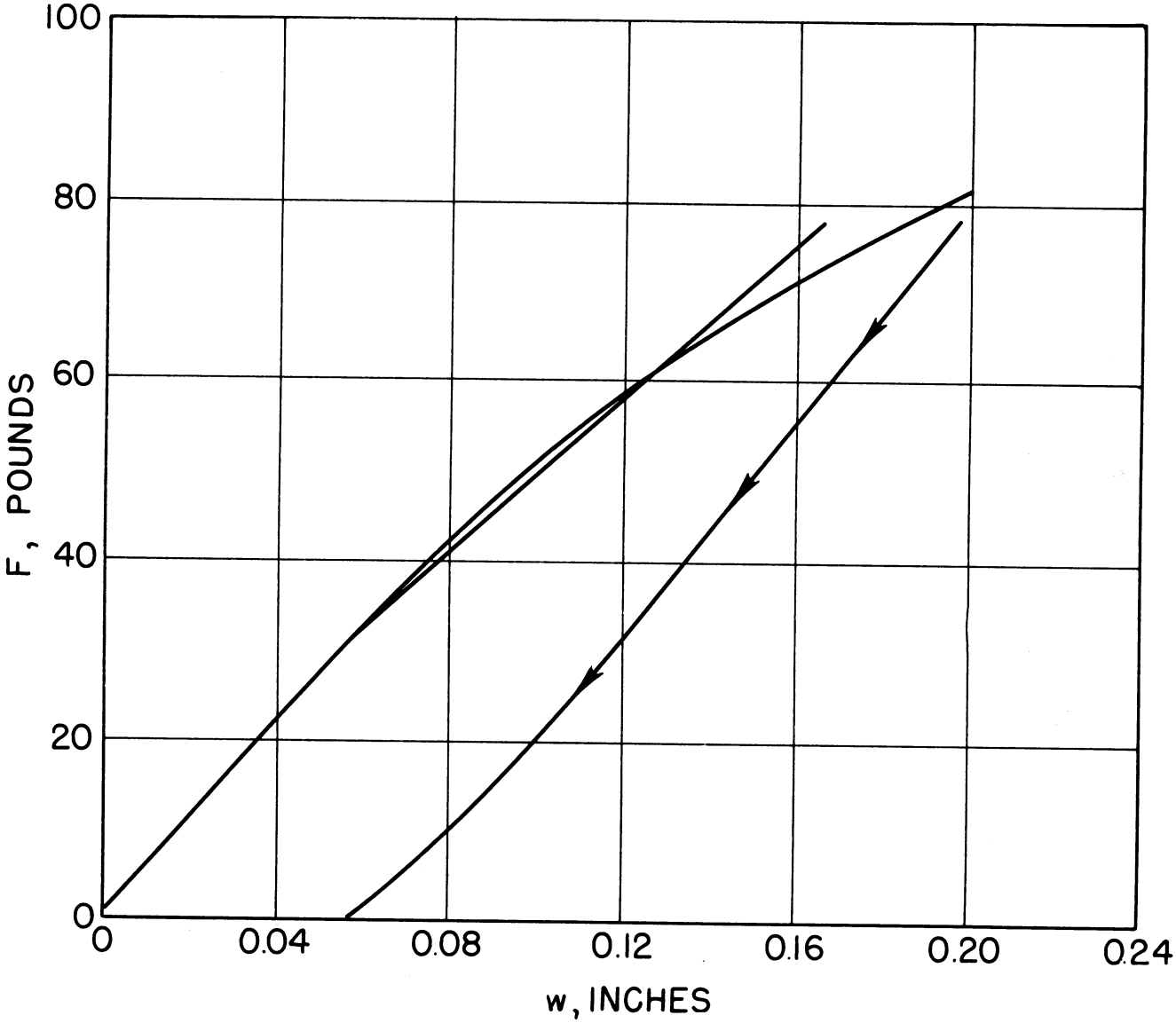

Figure 25. Load-Deflection Curve for Zamak-3 Cantilever Beam (ZAB-2)

unloading should occur when the load has decreased by an amount equal to two times the initial load or 2x1.5 F_e. This should be a drop of 60 pounds. Yielding during unloading should take place then at 22 pounds, a value in good agreement with that observed.

Figure 26 shows the initial portion of the load-tip deflection and load-root strain curves for another Zamak-3 beam. In this case the value of F_e from the load-root strain curve is about 18 pounds. The load-tip deflection curve deviates from linearity or shows gross yielding at a load of about 29 pounds, which is 1.61 times the experimental F_e. Again the slope of the elastic portion of the curve of load versus tip deflection is very near to the predicted value.

Figure 27 presents the entire load-tip deflection curve for the specimen of Figure 26. Again the linear load-deflection relation after yielding is a reasonably good approximation for tip deflections less than 0.14 inch or loads of less than 63 pounds. The maximum load reached for this specimen was 97 pounds and unloading from that point is linearly elastic until the load has decreased to 33 pounds. Thus the load decreased 64 pounds before yielding occurred which is near to the theoretical decrease of 60 pounds.

In summary the two typical Zamak-3 beams which were tested as cantilevers give results which are in reasonably good agreement with theory. A theoretical load-tip deflection relationship based on elastic-linear strain hardening behavior gives good predictions for the initial plastic range up to loads which are about three times the load at first yielding in the outer fibers. Kinematic hardening theory adequately predicts the point of yielding on unloading. The latter is in agreement with data reported earlier in WADD-TR-60-869 and reinforces the earlier data with results from an entirely different test situation.

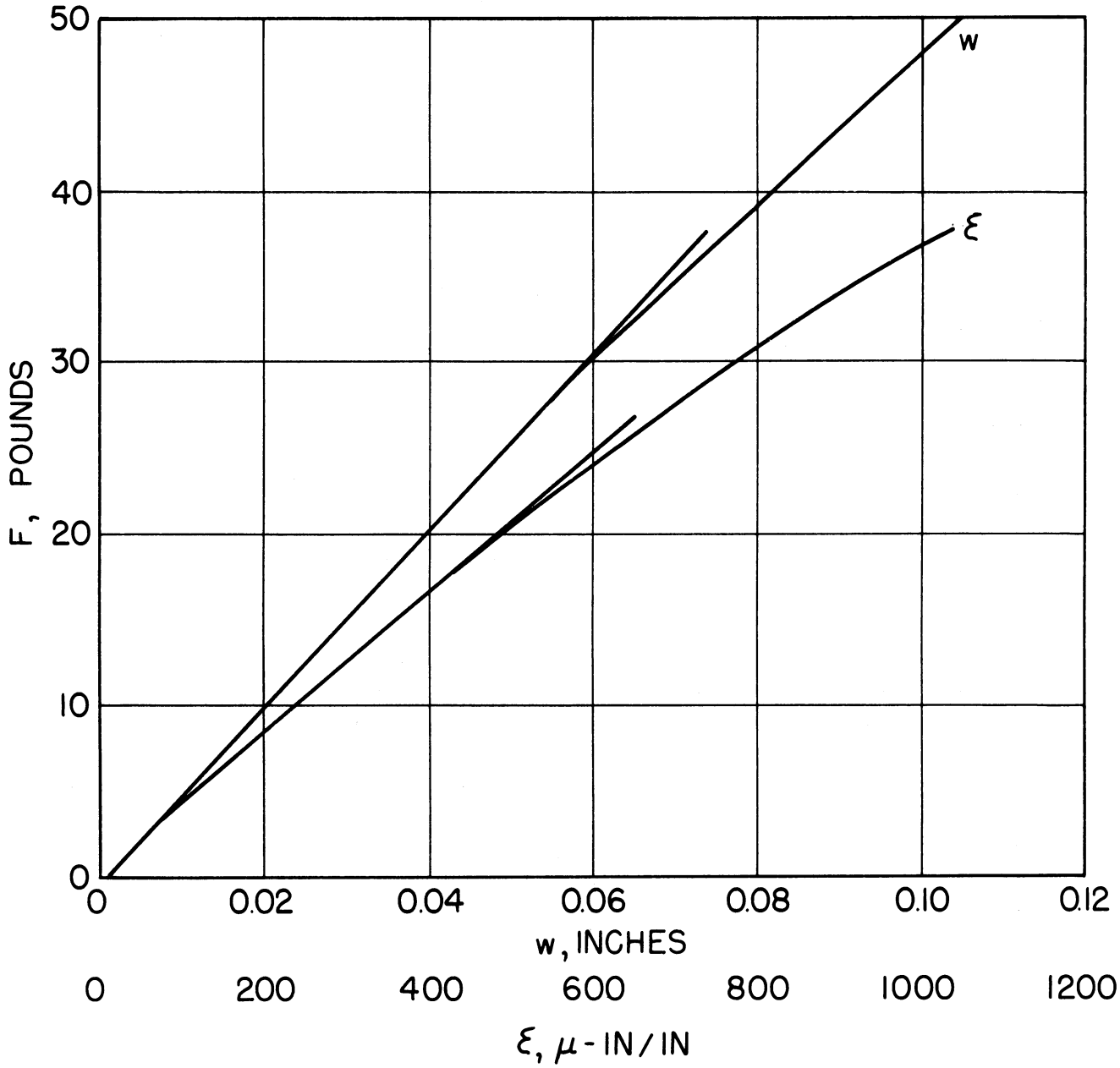

Figure 26. Load-Deflection and Load-Strain Curves for Zamak-3 Cantilever Beam (ZAB-3)

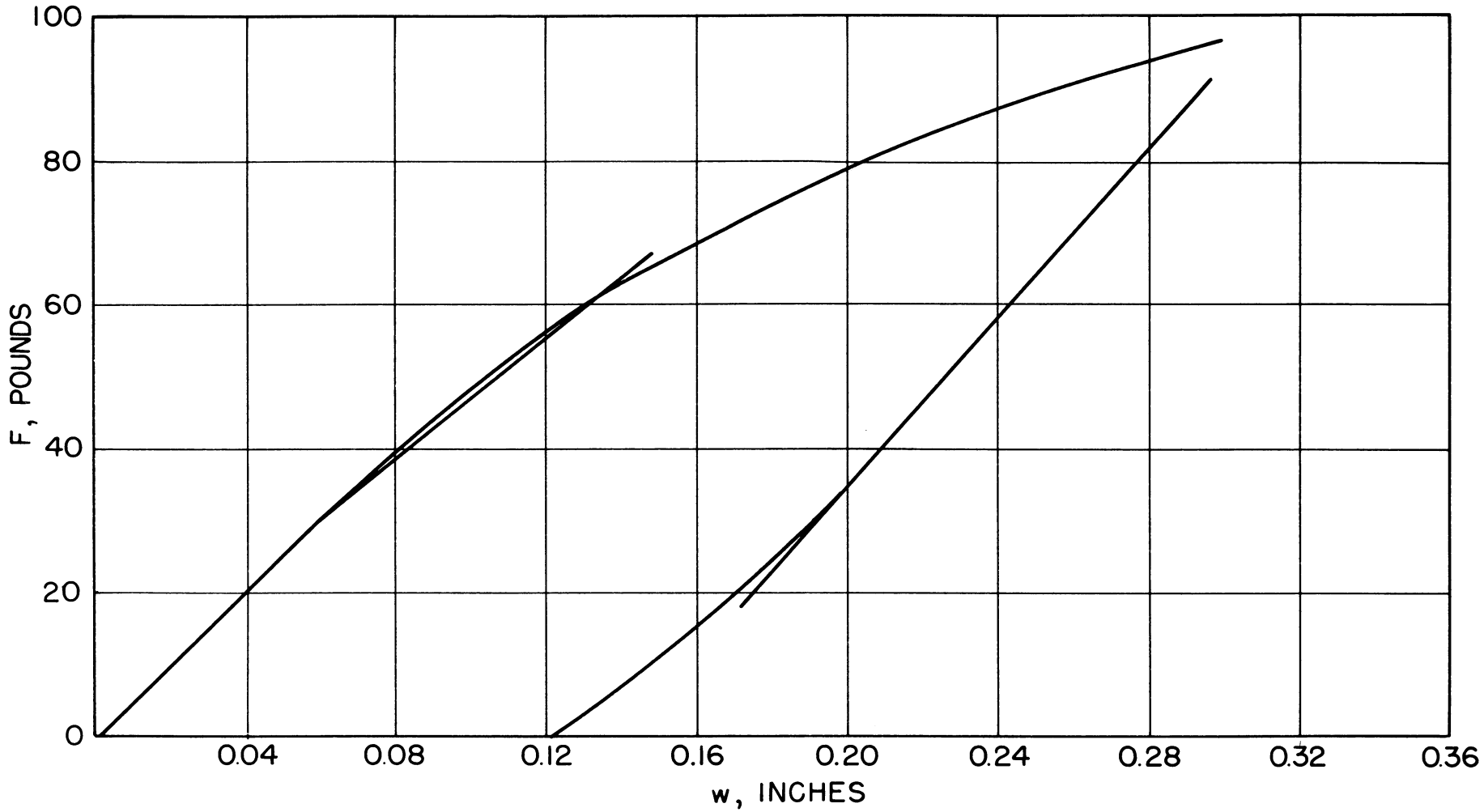

Figure 27. Load-Deflection Curve for Zamak-3 Cantilever Beam (ZAB-3)

REFERENCES

1. Haythornthwaite, R. M. and Jenkins, D. R., Effect of State of Stress on the Failure of Metals at Various Temperatures, Technical Documentary Report No. WADD-TR-60-869, Part II, June, 1962.

2. Clark, S. K., Gascoigne, H. E., Jenkins, D. R., and Wolf, L. W., Effect of State of Stress on the Failure of Metals at Various Temperatures, Summary Technical Report, WADD-TR-60-234, March, 1960.

3. Haythornthwaite, R. M., "Range of Yield Condition in Ideal Plasticity," Journal of the Engineering Mechanics Division, Proceedings of the American Society of Civil Engineers, Vol. 87, No. EM6, December, 1961.

4. Hill, R., The Mathematical Theory of Plasticity, Oxford University Press, 1950, p. 106.

5. Prager, W., "The Theory of Plasticity: A Survey of Recent Achievements," Proceedings of the Institution of Mechanical Engineers, Vol. 169, 1955, pp. 41-57.

6. Griffith, A. A., "The Theory of Rupture," Proceedings of the First International Congress for Applied Mechanics, (Delft), 1924, pp. 55-63.